AD-A280 573

Quarterly Technical Report

Solid State Research

DTIC
ELECTE
JUN 23 1994
S F D

DTIC QUALITY INSPECTED 2

1993:4

Lincoln Laboratory

MASSACHUSETTS INSTITUTE OF TECHNOLOGY

LEXINGTON, MASSACHUSETTS

Prepared for the Department of the Air Force under Contract F19628-90-C-0002.

Approved for public release; distribution is unlimited.

94-19215

94 6 22 122

This report is based on studies performed at Lincoln Laboratory, a center for research operated by Massachusetts Institute of Technology. The work was sponsored by the Department of the Air Force under Contract F19628-90-C-0002.

This report may be reproduced to satisfy needs of U.S. Government agencies.

The ESC Public Affairs Office has reviewed this report, and it is releasable to the National Technical Information Service, where it will be available to the general public, including foreign nationals.

This technical report has been reviewed and is approved for publication.

FOR THE COMMANDER

Gary Tutungian
Administrative Contracting Officer
Contracted Support Management

Non-Lincoln Recipients

PLEASE DO NOT RETURN

Permission is given to destroy this document when it is no longer needed.

MASSACHUSETTS INSTITUTE OF TECHNOLOGY
LINCOLN LABORATORY

SOLID STATE RESEARCH

QUARTERLY TECHNICAL REPORT

1 AUGUST — 31 OCTOBER 1993

ISSUED 22 APRIL 1994

Accesion For	
NTIS CRA&I	☑
DTIC TAB	☐
Unannounced	☐
Justification	
By	
Distribution /	
Availability Codes	
Dist	Avail and / or Special
A-1	

Approved for public release; distribution is unlimited.

LEXINGTON MASSACHUSETTS

ABSTRACT

This report covers in detail the research work of the Solid State Division at Lincoln Laboratory for the period 1 August through 31 October 1993. The topics covered are Electrooptical Devices, Quantum Electronics, Materials Research, Submicrometer Technology, High Speed Electronics, Microelectronics, and Analog Device Technology. Funding is provided primarily by the Air Force, with additional support provided by the Army, ARPA, Navy, BMDO, and NASA.

TABLE OF CONTENTS

	Abstract	iii
	List of Illustrations	vii
	List of Tables	x
	Introduction	xi
	Reports on Solid State Research	xiii
	Organization	xxi
1.	ELECTROOPTICAL DEVICES	1
1.1	$InAs_{1-x}Sb_x/In_{1-y}Ga_yAs$ Multiple-Quantum-Well Heterostructures for Improved 4–5-μm Lasers	1
2.	QUANTUM ELECTRONICS	7
2.1	$Tm:YVO_4$ Microchip Laser	7
2.2	Single-Mode Diode-Pumped $Nd:YVO_4$ Microchip Laser with 240 mW of Output Power	10
2.3	Aperture Guiding in Quasi-Three-Level Lasers	11
3.	MATERIALS RESEARCH	15
3.1	High-Power GaInAsSb/AlGaAsSb Multiple-Quantum-Well Diode Lasers Emitting at 1.9 μm	15
3.2	Growth of Undoped and Se-Doped GaSb by Organometallic Vapor Phase Epitaxy	18
4.	SUBMICROMETER TECHNOLOGY	23
4.1	Mosaic Diamond Substrates Approaching Single-Crystal Quality Using Cube-Shaped Diamond Seeds	23
4.2	Resonant-Tunneling Transmission Lines	27
5.	HIGH SPEED ELECTRONICS	33
5.1	Effects of Resist Geometry on GaAs/AlGaAs Structures Etched with Angled Cl_2-IBAE	33
6.	MICROELECTRONICS	39
6.1	Wafer-Scale 1960 × 2560 Frame-Transfer CCD Imager	39
7.	ANALOG DEVICE TECHNOLOGY	43
7.1	Microwave Power-Handling Capability of Superconducting Planar Transmission Lines and Resonators	43

LIST OF ILLUSTRATIONS

Figure No.		Page
1-1	Flat band diagram of $InAs_{0.85}Sb_{0.15}/In_{0.84}Ga_{0.16}As$ multiple-quantum-well (MQW) heterostructure on InAs substrate (a) without and (b) with strain-induced bandedge shifts.	2
1-2	Calculated emission wavelength λ_g, valence-band barrier height ΔE_v, and valence subband splitting $E_{v1}-E_{v2}$ for a range of compositions for $InAs_{1-x}Sb_x/In_{1-y}Ga_yAs$ MQW heterostructure.	4
2-1	Polarization-resolved absorption spectra of $Tm:YVO_4$ with Tm concentration of 5 at.%.	7
2-2	Polarization-resolved fluorescence spectra of $Tm:YVO_4$ with Tm concentration of 5 at.%.	8
2-3	Dependence of $Tm:YVO_4$ microchip laser output power on incident pump power.	9
2-4	Dependence of $Nd:YVO_4$ microchip laser output power on incident pump power.	10
2-5	Schematic of Yb:YAG microchip laser experiment viewed in plane perpendicular to InGaAs diode laser junctions. The cylindrical lens collimates the light in the plane of the junction.`	12
2-6	Yb:YAG microchip laser output power and cavity mode radius as a function of incident pump power.	12
3-1	Room-temperature pulsed threshold current density vs inverse cavity length for 300-μm-wide GaInAsSb/AlGaAsSb quantum-well lasers.	16
3-2	Pulsed threshold current density vs heatsink temperature for quantum-well GaInAsSb/AlGaAsSb laser 1000 μm long.	16
3-3	Output power vs current for CW operation of 300-μm-wide by 1000-μm-long GaInAsSb/AlGaAsSb quantum-well laser.	17
3-4	GaSb growth rate dependence on inverse growth temperature.	18
3-5	Surface morphology of GaSb layers grown on GaAs substrates at 600°C and with V/III ratios of (a) 0.7, (b) 0.8, (c) 0.9, and (d) 1.0.	19
3-6	V/III ratio vs growth temperature for optimum surface morphology of GaSb layers grown on GaAs substrates.	20

LIST OF ILLUSTRATIONS (Continued)

Figure No.		Page
3-7	Hole concentration and mobility at 77 K for undoped GaSb layers as a function of growth temperature.	21
3-8	Electron concentration and mobility at 77 K for Se-doped GaSb layers as a function of growth temperature.	21
4-1	(a) Scanning electron micrograph (SEM) of a cubic diamond; the square faces of the cube are (100) planes and the corners are faced with (111) planes. (b) Higher-magnification SEM of the top right corner of the crystal in (a).	24
4-2	Optical micrograph of junction of two coalesced structures with different crystal orientations.	25
4-3	Distribution of in-plane orientation of diamond cubes after orientation with square frame (solid circles) and by pushing and deforming layer of cubes (open circles).	25
4-4	Distribution of tip angles between (100) planes and substrate surface as determined by x-ray diffraction.	26
4-5	Resonant-tunneling diode (RTD) circuits demonstrating bistable operation. (a) Diagram and (b) current-voltage (I-V) characteristic for RTD with resistive load. (c) Diagram and (d) I-V characteristic for RTD with smaller RTD load. In (b) and (d) the dashed lines indicate load lines. For both (b) and (d) the intersections of the load lines with the device characteristics determine the possible operating points (labeled I, II, and III) for the circuits.	28
4-6	Bistable transmission line suitable for logic interconnect or pulse shaping.	29
4-7	Computer simulation of ten-stage bistable transmission-line structure showing pulse shaping. In this simulation $Z_0 = 50\ \Omega$ and $R_{term} = 50\ \Omega$. The effective propagation velocity is 8.3×10^9 cm s^{-1}, the series resistive loss is 2.4×10^2 Ω cm^{-1}, and the length of each segment is 0.2 cm.	29
4-8	Sketch of proposed implementation of RTD transmission line.	30
5-1	Sketches and scanning electron micrographs (SEMs) showing important resist parameters and their effect on the etching process. (a) Diagram and (b) SEM showing resist edge ripple and sloped sidewalls; also seen in (a) is an extraneous foot. (c) Diagram and (d) SEM showing edge erosion and edge ripple produced in the GaAs after etching the structure in (a).	34

LIST OF ILLUSTRATIONS (Continued)

Figure No.		Page
5-2	SEMs of (a) AZ5214E resist printed using chlorine ion-beam-assisted etching (Cl_2-IBAE) techniques and (b) sidewall of structure etched using the resist as a mask.	35
5-3	Schematic diagrams showing effect of resist geometry on Cl_2-IBAE etching of small structures. In (a) reflected ions do not significantly contribute to the sidewall slope, as compared to (b) where they aid in forming a structure useful in vacuum-microelectronics applications.	36
5-4	SEMs demonstrating ability of Cl_2-IBAE system to etch the structures illustrated in Figure 5-4. Shown are structures obtained using (a) angled etching with a rounded-edge resist, (b) angled etching with a vertical-edge resist whose thickness was greater than the resist opening, and (c) normal-incidence etching with a resist whose thickness was greater than the resist openings. In (b) a 200-nm-wide resist opening was used to produce the 80-nm-wide etched opening.	36
6-1	Schematic of 1960 × 2560-pixel frame-transfer charge-coupled device imager. This device fills almost all the usable area of a 100-mm-diam silicon wafer.	40
6-2	Photograph of completed device wafer. Small test structures are located around the periphery of the imager.	41
7-1	Geometries of superconducting resonators: (a)–(c) Cross-sectional views of linear half-wavelength resonators and (d) rotated view of microstrip disk resonator.	43

LIST OF TABLES

Table No.		Page
1-1	Physical Parameter Values of $InAs_{0.85}Sb_{0.15}$ and $In_{0.84}Ga_{0.16}As$ Alloys Interpolated from Corresponding Binary Compounds	3
2-1	Cavity Mode Radius Predictions from Fast Fourier Transform Calculations	13
7-1	Parameters for Transmission Lines and Resonating Structures	44
7-2	Relative Power-Handling Capability of Superconducting Transmission Lines	45
7-3	Quality Factor and Power-Handling Capability of Superconducting Resonating Structures with $f_0 = 2$ GHz	46

INTRODUCTION

1. ELECTROOPTICAL DEVICES

A new strained-layer multiple-quantum-well heterostructure has been proposed that reduces threshold carrier density and Auger recombination in 4–5-μm lasers. This system shows considerable promise for favorable band alignment, adequate carrier confinement, sufficient valence subband separation, and high-quality epitaxial growth.

2. QUANTUM ELECTRONICS

When pumped with a 1-W laser diode, a Tm:YVO_4 microchip laser has produced 150 mW of 1.94-μm output in a near-diffraction-limited beam at room temperature. Using a Ti:Al_2O_3 laser as the pump and reducing the temperature of the Tm:YVO_4 from 20 to −30°C resulted in no measurable change in threshold and increased the slope efficiency by only 20%.

A diode-pumped Nd:YVO_4 microchip laser has been constructed. This laser has produced 240 mW of single-frequency output in a near-diffraction-limited beam.

Aperture guiding, as opposed to thermal waveguiding, has been shown to be the dominant mechanism for cavity mode stabilization in a quasi-three-level Yb:YAG laser in a flat-flat resonator. Excellent agreement was obtained between the experimental and modeled spot size in this laser when aperture guiding was included in the model.

3. MATERIALS RESEARCH

Significant improvements have been made in the performance of GaInAsSb/AlGaAsSb multiple-quantum-well diode lasers emitting at 1.91 μm. Threshold current densities as low as 143 A/cm^2, single-ended CW output powers as high as 1.3 W, and power efficiencies > 15% have been achieved at 12°C.

GaSb epilayers have been grown by low-pressure organometallic vapor phase epitaxy with layers unintentionally doped *p*-type, yielding hole concentrations and hole mobilities measured at 77 K in the ranges $1–2 \times 10^{16}$ cm^{-3} and $2.5–3.8 \times 10^3$ cm^2/V s, respectively. With *n*-type doping of GaSb using H_2Se, doping efficiency increased with decreasing substrate temperature and, at the lowest growth temperature of 580°C, resulted in an electron concentration measured at 77 K of 4.9×10^{17} cm^{-3} with a corresponding mobility of 1.5×10^3 cm^2/V s.

4. SUBMICROMETER TECHNOLOGY

In an improved method of forming mosaic diamond substrates from single cubic subcrystals, alignment of randomly oriented cubes in an array has been accomplished by displacing and reforming the array. Depending upon the techniques used, orientation with a standard deviation from 1° to 5° can be achieved.

High-speed waveforming circuits have been designed using resonant-tunneling diodes and high-frequency transmission lines. A monolithic GaAs/AlGaAs resonant-tunneling transmission line has been simulated for operation at 5 GHz.

5. HIGH SPEED ELECTRONICS

Etch-specific resist geometries have been developed for Cl_2-based ion-beam-assisted etching in order to optimize sidewall smoothness at a variety of sidewall angles and to demonstrate a new process that allows the width of the etched opening to be significantly smaller than that of the resist opening. Etched slots 80 nm wide have been produced with electron-beam resist openings of 200 nm.

6. MICROELECTRONICS

A 1960 × 2560-pixel, frame-transfer charge-coupled device imager has been designed that occupies an entire 100-mm-diam silicon wafer. The first lot of wafers has been fabricated, and preliminary yield data indicated that more than a third of the devices are free of fatal shorts.

7. ANALOG DEVICE TECHNOLOGY

Numerical methods for electromagnetic analysis have been used to accurately determine current density distributions and peak magnetic fields in superconducting planar transmission lines. The power-handling capability calculated for a circular microstrip disk resonator was found to be significantly higher than for stripline, microstrip, and coplanar transmission line resonators.

REPORTS ON SOLID STATE RESEARCH

1 AUGUST THROUGH 31 OCTOBER 1993

PUBLICATIONS

Monolithic Optoelectronic Transistor: A New Smart-Pixel Device	B. F. Aull K. B. Nichols P. A. Maki S. C. Palmateer E. R. Brown T. A. Lind	*Appl. Phys. Lett.* **63**, 1555 (1993)
Application of Radiative Renormalization to Strong-Field Resonant Nonlinear Optical Interactions	O. Blum* P. Harshman* T. K. Gustafson* P. L. Kelley	*Phys. Rev. A* **47**, 5165 (1993)
Strong Intersubband Absorption by Photogenerated Carriers in Quantum Wells	E. R. Brown K. A. McIntosh K. B. Nichols	*Proc. SPIE* **1675**, 260 (1992)
Heat Generation in Nd:YAG and Yb:YAG	T. Y. Fan	*IEEE J. Quantum Electron.* **29**, 1457 (1993)
High-Conductance, Low-Leakage Diamond Schottky Diodes	M. W. Geis N. N. Efremow J. A. von Windheim*	*Appl. Phys. Lett.* **63**, 952 (1993)
Comparison of Liquid- and Vapor-Phase Silylation Processes for 193-nm Positive-Tone Lithography	M. A. Hartney R. R. Kunz L. M. Eriksen D. C. LaTulipe*	*Proc. SPIE* **1925**, 270 (1993); *Opt. Eng.* **32**, 2382 (1993)
Comparison of Etching Tools for Resist Pattern Transfer	M. W. Horn M. A. Hartney R. R. Kunz	*Opt. Eng.* **32**, 2388 (1993)

*Author not at Lincoln Laboratory.

Acid-Catalyzed Single-Layer Resists for ArF Lithography	R. R. Kunz R. D. Allen* W. D. Hinsberg* G. M. Wallraff*	*Opt. Eng.* **32**, 2363 (1993)
Experiment and Simulation of Sub-0.25-μm Resist Processes for 193-nm Lithography	R. R. Kunz M. A. Hartney R. W. Otten, Jr. E. Barouch* U. Hollerbach*	*Proc. SPIE* **1927** (Pt 2), 464 (1993)
Design of Acid-Catalyzed Single-Layer Resists for ArF Lithography	R. R. Kunz G. M. Wallraff* R. D. Allen* W. D. Hinsberg*	*Proc. SPIE* **1925**, 167 (1993)
Diode-Laser-Pumped InGaAs/GaAs/AlGaAs Heterostructure Lasers with Low Internal Loss and 4-W Average Power	H. Q. Le W. D. Goodhue P. A. Maki S. DiCecca	*Appl. Phys. Lett.* **63**, 1465 (1993)
Demonstration of a 3-GHz-Bandwidth Real-Time Spectral-Analysis Receiver Based on a High-T_c Superconductive Chirp Filter	W. G. Lyons M. M. Seaver D. R. Arsenault R. R. Boisvert T. C. L. G. Sollner	*Microwave Opt. Technol.* **6**, 728 (1993)
High Power Microwave Filters	R. W. Ralston D. E. Oates A. C. Anderson W. G. Lyons	*4th International Superconductive Electronics Conference, Extended Abstracts* (Centennial Conferences, Boulder, Colo., 1993), p. 48
Laser-Induced Damage in Pellicles at 193 nm	M. Rothschild J. H. C. Sedlacek	*Opt. Eng.* **32**, 2421 (1993)
Three-Wavelength Interconversion Laser	P. A. Schulz T. H. Jeys	*Opt. Lett.* **18**, 1630 (1993)

*Author not at Lincoln Laboratory.

A Wideband Real-Time Spectrum Analyzer Using a High-T_c Superconducting Chirp Filter	T. C. L. G. Sollner W. G. Lyons D. R. Arsenault M. M. Seaver R. R. Boisvert	*4th International Superconductive Electronics Conference, Extended Abstracts* (Centennial Conferences, Boulder, Colo., 1993), p. 5
Effect of Back Contact Impedance on Frequency Dependence of Capacitance-Voltage Measurements on Metal/Diamond Diodes	V. Venkatesan* K. Das* J. A. von Windheim* M. W. Geis	*Appl. Phys. Lett.* **63**, 1065 (1993)
Multiquantum-Well Detection of Nanosecond Far-Infrared Superradiant Pulses at Temperatures above 77 K	J. Waldman* D. B. Moix* D. P. Scherrer* F. K. Kneubuhl* W. D. Goodhue E. R. Mueller* M. J. Coulombe*	*Infrared Phys.* **33**, 487 (1992)
A Ti:Al_2O_3 Master-Oscillator/Power-Amplifier System	K. F. Wall P. A. Schulz R. L. Aggarwal P. Lacovara A. Sanchez	*IEEE J. Quantum Electron.* **29**, 1505 (1993)

ACCEPTED FOR PUBLICATION

Effects of Annealing on Photorefractive Damage in Titanium-Indiffused $LiNbO_3$ Modulators	G. E. Betts F. J. O'Donnell K. G. Ray	*IEEE Photon. Technol. Lett.*
Effect of Lattice Mismatch on InAs/AlSb Resonant-Tunneling Diodes	E. R. Brown S. J. Eglash G. W. Turner C. D. Parker J. V. Pantano D. R. Calawa	*IEEE Trans. Electron Devices*

*Author not at Lincoln Laboratory.

Effect of Surface Termination on a Photonic-Crystal Planar-Dipole Antenna	E. R. Brown C. D. Parker	*Appl. Phys. Lett.*
CCD Soft X-Ray Imaging	B. E. Burke	*IEEE Trans. Nucl. Sci.*
Single-Frequency GaInAsSb/AlGaAsSb Quantum-Well Ridge-Waveguide Lasers Emitting at 2.1 μm	H. K. Choi S. J. Eglash M. K. Connors	*Appl. Phys. Lett.*
GaInAsSb-AlGaAsSb Tapered Lasers Emitting at 2 μm	H. K. Choi J. N. Walpole G. W. Turner S. J. Eglash L. J. Missaggia M. K. Connors	*IEEE Photon. Technol. Lett.*
CW Operation of Monolithic Arrays of Surface-Emitting AlGaAs Diode Lasers with Dry-Etched Vertical Facets and Parabolic Deflecting Mirrors	J. P. Donnelly W. D. Goodhue C. A. Wang R. J. Bailey G. A. Lincoln G. D. Johnson L. J. Missaggia J. N. Walpole	*IEEE Photon. Technol. Lett.*
Quasi-Three-Level Lasers	T. Y. Fan	In *Solid-State Lasers: New Developments and Applications* (Plenum, New York)
Controlled *p*-Type Sb Doping in LPE-Grown $Hg_{1-x}Cd_xTe$	T. C. Harman	*J. Electron. Mater.*
Use of Quantum-Well Superlattices to Obtain a High Figure of Merit from Nonconventional Thermoelectric Materials	L. D. Hicks* T. C. Harman M. S. Dresselhaus*	*Appl. Phys. Lett.*

*Author not at Lincoln Laboratory.

Integrated AlGaAs Waveguide Components for Optical Phase Difference Measurement and Correction	S. D. Lau* J. P. Donnelly C. A. Wang R. H. Rediker*	*IEEE J. Quantum Electron.*
A Vertical Schottky-Gated Resonant Tunneling Transistor with High Transconductance at Room Temperature	W. C. B. Peatman* E. R. Brown M. J. Rooks* P. A. Maki M. Shur*	*IEEE Electron Device Lett.*

PRESENTATIONS†

Fabrication and Performance of a Monolithic Optoelectronic Transistor	K. B. Nichols B. F. Aull P. A. Maki S. C. Palmateer E. R. Brown T. A. Lind B. F. Gramstorff	IEEE/Cornell Conference on Advanced Concepts in High Speed Semiconductor Devices and Circuits, Ithaca, New York, 2-4 August 1993
Schottky-Gated Resonant Tunneling Transistors	W. C. B. Peatman* M. J. Rooks* E. R. Brown M. Shur* P. A. Maki	
Diamond Transistor Performance and Fabrication	M. W. Geis J. C. Twichell	2nd International Conference on the Applications of Diamond Films and Related Materials, Saitama, Japan, 25-27 August 1993

*Author not at Lincoln Laboratory.

†Titles of presentations are listed for information only. No copies are available for distribution.

Opportunities and Issues for High-T_c Microwave Devices and Subsystems	W. G. Lyons	2nd Taiwan International Conference on Superconductors, Sun-Moon Lake, Taiwan, 27-30 August 1993
CO_2-Laser Heterodyne Detection with a GaAs/AlGaAs MQW Structure	E. R. Brown K. A. McIntosh K. B. Nichols F. W. Smith M. J. Manfra	NATO Advanced Research Workshop on Quantum Well Intersubband Transitions, Whistler, British Columbia, 7-10 September 1993
Monolithic Optoelectronic Transistor in AlGaAs-GaAs Grown by Gas-Source Molecular Beam Epitaxy	P. A. Maki S. C. Palmateer K. B. Nichols E. R. Brown T. A. Lind B. F. Aull	North American Conference on Molecular Beam Epitaxy, Stanford, California, 13-15 September 1993
MBE Growth of High-Performance Mid-Infrared Diode Lasers	G. W. Turner H. K. Choi D. R. Calawa J. V. Pantano J. W. Chludzinski	
Applications of Lasers in Microelectronics and Micromechanics	D. J. Ehrlich	NATO Advanced Study Institute on Excimer Lasers and Applications, Elounda, Greece, 14 September 1993
Diamond Field-Emission Cathodes	J. C. Twichell M. W. Geis C. O. Bozler D. D. Rathman N. N. Efremow K. E. Krohn M. A. Hollis T. M. Lyszczarz R. Uttaro M. Kordesch* K. Okano*	4th European Conference on Diamond, Diamond-Like and Related Materials, Albufeira, Portugal, 20-24 September 1993

*Author not at Lincoln Laboratory.

Quantum Well Nonlinearities for Optical Communication Applications	H. Q. Le	Seminar, Tufts University, Medford, Massachusetts, 27 September 1993
High-T_c Compressive Receiver System for Wideband Real-Time Spectral Analysis	W. G. Lyons D. R. Arsenault M. M. Seaver R. R. Boisvert T. C. L. G. Sollner	Workshop on Superconductive Electronics: Devices, Circuits and Systems, Ogunquit, Maine, 3-7 October 1993
CCD Soft X-Ray Imagers for ASCA and AXAF	B. E. Burke R. W. Mountain P. J. Daniels M. Cooper V. S. Dolat	Seminar, Max-Planck Institute, Munich, Germany, 4 October 1993
Large-Area Imager Development at MIT Lincoln Laboratory	B. E. Burke	European Southern Observatory Workshop on Large-Size CCDs, Garching, Germany, 4-5 October 1993
Fabrication and Performance of Gated Field-Emitter Arrays Having 0.32-mm Tip-to-Tip Spacings	C. O. Bozler C. T. Harris S. Rabe D. D. Rathman W. D. Goodhue M. A. Hollis H. I. Smith*	Electrochemical Society Symposium, New Orleans, Louisiana, 11-12 October 1993
Prototyping to Manufacturing: Applications of Lasers in Microelectronics	D. J. Ehrlich	1st International Conference on Photo-Excited Processes and Applications, Sendai, Japan, 13-15 October 1993
Single-Spatial-Mode Tapered Amplifiers and Oscillators	J. N. Walpole	Seminar, Massachusetts Institute of Technology, Cambridge, Massachusetts, 14 October 1993

*Author not at Lincoln Laboratory.

Diamond Transistor Performance and Fabrication	M. W. Geis J. C. Twichell	IEEE Electron Devices Meeting, Lexington, Massachusetts, 20 October 1993
Charge-Coupled Device Detection of ^{32}P for DNA Hybridization Sequencing	R. K. Reich J. B. Lamture* M. E. Hogan* K. L. Beattie* B. E. Burke M. D. Eggers* D. J. Ehrlich M. A. Hollis B. B. Kosicki S. R. Smith* R. S. Varma*	International Workshop on Sequencing by Hybridization, The Woodlands, Texas, 29-30 October 1993

*Author not at Lincoln Laboratory.

ORGANIZATION

SOLID STATE DIVISION

A. L. McWhorter, *Head*
I. Melngailis, *Associate Head*
E. Stern, *Associate Head*
D. C. Shaver, *Assistant Head*
J. F. Goodwin, *Assistant*

D. J. Ehrlich, *Senior Staff*
N. L. DeMeo, Jr., *Associate Staff*
J. W. Caunt, *Assistant Staff*
K. J. Challberg, *Administrative Staff*

SUBMICROMETER TECHNOLOGY

M. Rothschild, *Leader*
T. M. Lyszczarz, *Assistant Leader*

Astolfi, D. K.
Craig, D. M.
Dennis, C. L.
DiNatale, W. F.
Doran, S. P.
Dubois, L. H.
Efremow, N. N., Jr.
Forte, A. R.
Geis, M. W.
Goodman, R. B.
Hartney, M. A.
Horn, M. W.
Keast, C. L.
Kunz, R. R.
Maki, P. A.
Melngailis, J.†
Palmateer, S. C.
Sedlacek, J. H. C.
Stern, M. B.
Uttaro, R. S.
Twichell, J. C.

QUANTUM ELECTRONICS

A. Sanchez-Rubio, *Leader*
T. Y. Fan, *Assistant Leader*

Aggarwal, R. L.
Cook, C. C.
Daneu, V.
DeFeo, W. E.
DiCecca, S.
Dill, C. D., III
Hotaling, T. C.
Hsu, L.*
Jeys, T. H.
Kelley, P. L.‡
Le, H. Q.
Nabors, C. D.
Ochoa, J. R.
Zayhowski, J. J.

ELECTRONIC MATERIALS

B-Y. Tsaur, *Leader*
D. L. Spears, *Assistant Leader*

Chen, C. K.
Choi, H. K.
Connors, M. K.
Fahey, R. E.
Finn, M. C.
Golovchenko, P. A.†
Harman, T. C.
Iseler, G. W.
Krohn, L., Jr.
McGilvary, W. L.
Nitishin, P. M.
Pantano, J. V.
Paul, S. A.*
Reinold, J. H., Jr.
Turner, G. W.
Wang, C. A.

HIGH SPEED ELECTRONICS

R. A. Murphy, *Leader*
M. A. Hollis, *Assistant Leader*

Bozler, C. O.
Brown, E. R.
Chen, C. L.
Clifton, B. J.‡
Goodhue, W. D.
Harris, C. T.
Lincoln, G. A., Jr.
Mahoney, L. J.
Manfra, M. J.
Mathews, R. H.
Mattia, J. P.*
McIntosh, K. A.
Nichols, K. B.
Parker, C. D.
Rabe, S.
Rathman, D. D.

* Research Assistant
† Part Time
‡ Leave of Absence

ELECTROOPTICAL DEVICES

R. C. Williamson, *Leader*
L. M. Johnson, *Assistant Leader*

Aull, B. F.
Bailey, R. J.
Betts, G. E.
Donnelly, J. P.
Golubovic, B.*
Groves, S. H.
Hovey, D. L.
Liau, Z. L.
Lind, T. A.
Missaggia, L. J.
Mull, D. E.
O'Donnell, F. J.
Palmacci, S. T.
Reeder, R. E.
Roussell, H. V.
Tsang, D. Z.
Walpole, J. N.
Woodhouse, J. D.

ANALOG DEVICE TECHNOLOGY

R. W. Ralston, *Leader*
T. C. L. G. Sollner, *Assistant Leader*
P. M. Mankiewich, *Assistant Leader*
A. C. Anderson, *Senior Staff*
A. M. Chiang, *Senior Staff*

Abusch, D. M.*
Arsenault, D. R.
Boisvert, R. R.
Brogan, W. T.
Delin, K. A.
Denneno, J. M.
Fitch, G. L.
Green, J. B.‡
Holtham, J. H.
LaFranchise, J. R.
Linden, D. S.*
Lyons, W. G.
Macedo, E. M., Jr.
Murphy, P. G.
Oates, D. E.
Sage, J. P.
Seaver, M. M.
Slattery, R. L.
Tam, K.*

MICROELECTRONICS

E. D. Savoye, *Leader*
B. B. Kosicki, *Assistant Leader*
B. E. Burke, *Senior Staff*

Clark, H. R., Jr.
Daniels, P. J.
Doherty, C. L., Jr.
Dolat, V. S.
Donahue, T. C.
Felton, B. J.
Gregory, J. A.
Johnson, K. F.
Loomis, A. H.
McGonagle, W. H.
Mountain, R. W.
Percival, K. A.
Reich, R. K.
Thomas, J. W.*
Young, D. J.

* Research Assistant
‡ Leave of Absence

1. ELECTROOPTICAL DEVICES

1.1 $InAs_{1-x}Sb_x/In_{1-y}Ga_yAs$ MULTIPLE-QUANTUM-WELL HETEROSTRUCTURES FOR IMPROVED 4–5-μm LASERS

Diode lasers emitting at 4–5-μm wavelengths are of considerable interest for atmospheric transmission, molecular spectroscopy, eye-safe applications, and other uses. Unfortunately, severe Auger recombination is expected for the low bandgaps, and double-heterostructure lasers using $InAs_{0.91}Sb_{0.09}$ active layers have been limited to operation below 160 K [1]–[3]. Recent development of lattice-mismatched strained layers holds considerable promise for a reduced Auger rate by altered band structure and reduced threshold carrier density [4],[5]. However, the search for a suitable strained-layer quantum-well heterostructure for the 4–5-μm lasers has been severely hindered, in part by the comparably low lying valence bandedge of the $InAs_{1-x}Sb_x$ wells [6]–[9], which would result in the confinement of holes to $Al_uGa_{1-u}As_vSb_{1-v}$ barrier layers with compositions close to the GaSb end [10],[11]. A superlattice (type II) comprising ~ 2.5-nm-thick InAs and InGaSb multilayers has been suggested for increased radiative recombination in such staggered band alignment [12], but concerns still exist about good epitaxial growth of these very thin layers of wide compositional disparity [13].

Here, we propose a new multiple-quantum-well (MQW) heterostructure with $In_{1-y}Ga_yAs$ barrier layers for favorable band alignment and hole confinement to $InAs_{1-x}Sb_x$ wells. The potential for favorable alignment can be inferred from the still lower valence bandedge of GaAs, with the sequence being E_v(InSb) > E_v(InAs) > E_v(GaAs) [6]–[9]. Moreover, both of these ternary alloys have compositions close to InAs and are more thermodynamically stable than the GaInAsSb quaternary alloys [14]. This MQW is therefore potentially suitable for high-quality epitaxial growth.

The band diagram shown in Figure 1-1(a) of an $InAs_{0.85}Sb_{0.15}/In_{0.84}Ga_{0.16}As$ MQW on an InAs substrate does not include the strain-induced shifts and is obtained by using previously calculated bandgaps [14] and conduction bandedges linearly interpolated from those of the corresponding binary compounds [6]–[9]. The MQW needs to be relatively thick (~ 0.4 μm) for a sufficient optical confinement factor, and the well and barrier layers have been chosen for equal thickness but opposite strain for a balanced stress. The strain of 0.010 corresponds to a critical layer thickness of ~ 23 nm.

Effects of strain on the band structure can be calculated by using perturbation theory [15] with published values of the deformation potentials [15],[16]. The shift of conduction bandedge from E_c^0 to E_c is given by

$$E_c = E_c^0 + 2\left(\frac{C_{11} - C_{12}}{C_{11}}\right) a_c \varepsilon \quad , \tag{1.1}$$

where C_{11} and C_{12} are elastic stiffness constants, a_c is the conduction-band hydrostatic deformation potential, and ε is the strain. The physical parameter values of the present ternary alloys are interpolated from the corresponding binary compounds and are listed in Table 1-1. (Note that ε is positive for tensile

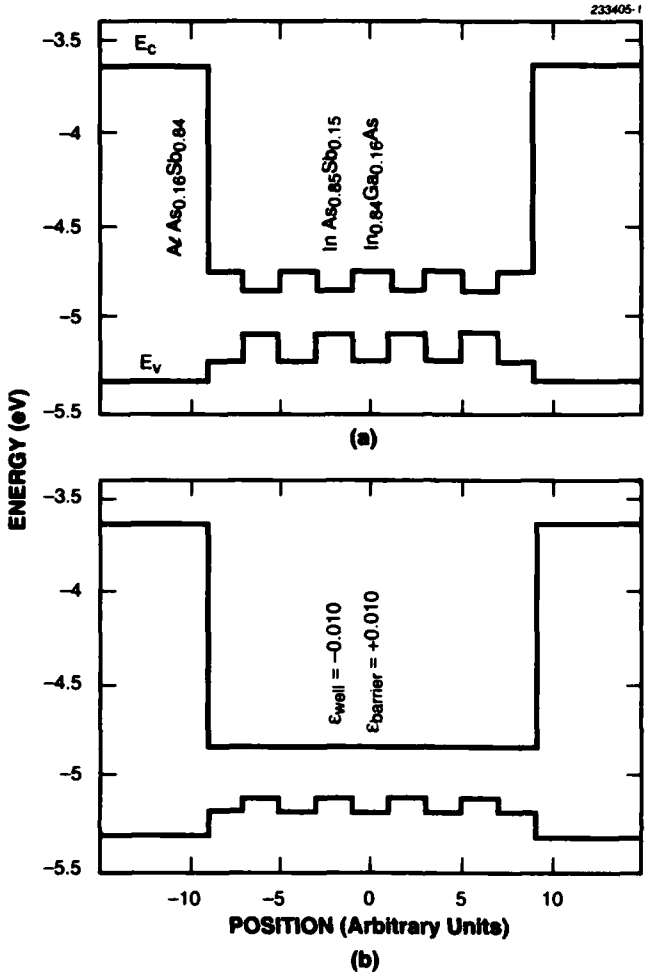

Figure 1-1. Flat band diagram of $InAs_{0.85}Sb_{0.15}/In_{0.84}Ga_{0.16}As$ multiple-quantum-well (MQW) heterostructure on InAs substrate (a) without and (b) with strain-induced bandedge shifts.

TABLE 1-1

Physical Parameter Values of $InAs_{0.85}Sb_{0.15}$ and $In_{0.84}Ga_{0.16}As$ Alloys Interpolated from Corresponding Binary Compounds

	GaAs	InAs	InSb	$InAs_{0.85}Sb_{0.15}$	$In_{0.84}Ga_{0.16}As$
E_c^0 (eV)	–4.06	–4.9	–4.5	–4.85	–4.77
E_v^0 (eV)	–5.48	–5.26	–4.76	–5.11	–5.24
C_{11} (10^{11} dyne cm^2)	12.3	8.6	6.7	8.32	9.18
C_{12} (10^{11} dyne cm^2)	5.7	4.8	3.7	4.64	4.94
a_c (eV)	–6.0	–4.4	–5.4	–4.55	–4.66
a_v (eV)	2.7	2.5	2.1	2.44	2.53
b (eV)	–1.7	–1.8	–2.0	–1.83	–1.78
ε	–	–	–	–0.010	0.010
E_c (eV)	–	–	–	–4.81	–4.81
E_{v1} (eV)	–	–	–	–5.10	–5.26
E_{v2} (eV)	–	–	–	–5.18	–5.18
	–	–	–		

strain and vice versa.) The biaxial strain splits the degeneracy (at E_v^0) of the heavy- and light-hole bands into E_{v1} and E_{v2}:

$$E_{v1} = E_v^0 + 2\left(\frac{C_{11} - C_{12}}{C_{11}}\right) a_v \varepsilon + \left(\frac{C_{11} + 2C_{12}}{C_{11}}\right) b\varepsilon \tag{1.2}$$

and

$$E_{v2} = E_v^0 + 2\left(\frac{C_{11} - C_{12}}{C_{11}}\right) a_v \varepsilon - \left(\frac{C_{11} + 2C_{12}}{C_{11}}\right) b\varepsilon \ . \tag{1.3}$$

where a_v is the valence-band hydrostatic deformation potential and b is the shear deformation potential. It should be noted that the E_{v1} subband has a smaller effective mass (i.e., is light-hole-like) in the junction plane and is desirable for lower threshold carrier density. This subband lies above the other one (E_{v2}) in the compressively strained InAsSb wells. The opposite is true for InGaAs barrier layers in tensile stress. The calculated band diagram including the shifts is shown in Figure 1-1(b).

Note that the strain causes significant shifts in the MQW bandedges. The valence-band offset is reduced to 0.08 eV, whereas the conduction-band offset virtually vanishes. This relatively small potential barrier nonetheless provides adequate carrier confinement for the present MQW. Because the wells and the barrier layers are of the same thickness, the carrier leakage to the barrier layers is primarily controlled by the Boltzmann factor $e^{-\Delta E_c/kT}$, which amounts to just 0.046 for ΔE_g of 0.08 eV and kT of 0.026 eV (for T of 300 K). (Note that there is no concern for carrier leakage to the Al-rich cladding layers because of their very wide bandgap.) The Coulomb attraction between the injected electrons and holes will further aid in their confinement. It should be noted that carrier confinement can be improved still more by adding some Al to the barrier layers.

An equally important issue is the separation of the two valence subbands in the wells, $E_{v1}-E_{v2}$, which determines the (unwanted) population of holes in the lower subband of E_{v2}. As can easily be seen from Equations (1.2) and (1.3), this separation is proportional to $|\varepsilon|$. For the present $|\varepsilon|$-value of 0.010, the energy separation $E_{v1}-E_{v2}$ is calculated to be 0.08 eV, which by coincidence is nearly equal to the valence-band offset between the wells and the barrier layers, and again corresponds to a Boltzmann factor of 0.05.

The bandgap of the $InAs_{0.85}Sb_{0.15}$ wells, calculated to be 0.29 eV, corresponds to an emission wavelength λ_g of 4.3 μm. The lasing wavelength will be somewhat shorter because of band filling. For a wider range of emission wavelengths, calculations have been carried out for varied well compositions and are summarized in Figure 1-2. (In these calculations, y_{Ga} is related to x_{Sb} through the condition of $\varepsilon_{well} = -\varepsilon_{barrier}$. In the parameter range of Figure 1-2, $\Delta E_v \approx E_{v1}-E_{v2}$ was obtained.) Similar calculations have also been performed for GaSb substrates. The larger lattice constant of GaSb requires a higher Sb

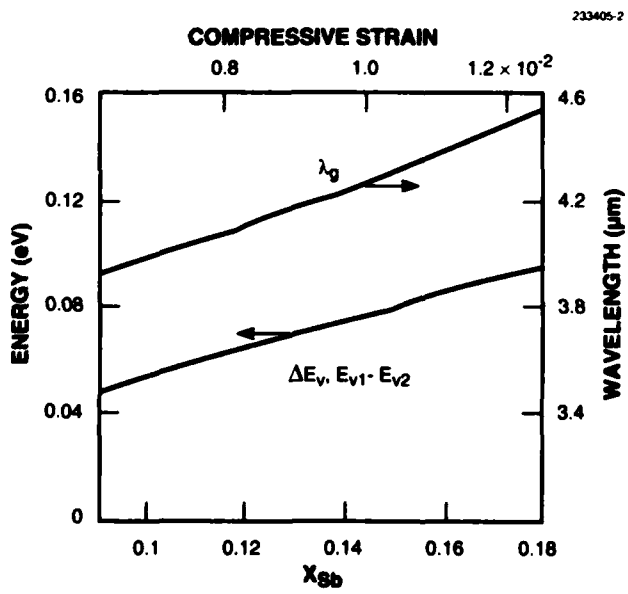

Figure 1-2. Calculated emission wavelength λ_g, valence-band barrier height ΔE_v, and valence subband splitting $E_{v1}-E_{v2}$ for a range of compositions for $InAs_{1-x}Sb_x/In_{1-y}Ga_yAs$ MQW heterostructure.

content in the wells in order to achieve a sufficient compressive strain. The emission wavelengths are therefore somewhat longer, in the 5-μm range. It should be noted, however, that the use of linearly interpolated physical parameter values has limited the accuracy in all of the present calculations.

Z. L. Liau
H. K. Choi

REFERENCES

1. J. P. van der Ziel, T. H. Chiu, and W. T. Tsang, *Appl. Phys. Lett.* **48**, 315 (1986).
2. S. J. Eglash and H. K. Choi, submitted to *Appl. Phys. Lett.*
3. H. Q. Le, G. W. Turner, S. J. Eglash, H. K. Choi, and D. A. Coppeta, submitted to *Appl. Phys. Lett.*
4. E. Yablonovitch and E. O. Kane, *J. Lightwave Technol.* **LT-4**, 504 (1986).
5. A. R. Adams, *Electron. Lett.* **22**, 249 (1986).
6. G. W. Gobeli and F. G. Allen, *Phys. Rev.* **137**, A245 (1965).
7. H. Sakaki, L. L. Chang, R. Ludeke, C-A. Chang, G. A. Sai-Halasz, and L. Esaki, *Appl. Phys. Lett.* **31**, 211 (1977).
8. F. L. Schuermeyer, P. Cook, E. Martinez, and J. Tantillo, *Appl. Phys. Lett.* **55**, 1877 (1989).
9. Y. Tsou, A. Ichii, and E. M. Garmire, *IEEE J. Quantum Electron.* **28**, 1261 (1992), and references therein.
10. H. K. Choi and S. J. Eglash, *IEEE J. Quantum Electron.* **27**, 1555 (1991); *Appl. Phys. Lett.* **59**, 1165 (1991); **61**, 1154 (1992).
11. S. J. Eglash and H. K. Choi, *Gallium Arsenide and Related Compounds 1991, Inst. Phys. Conf. Ser.* **120**, 487 (1992).
12. C. Mailhiot and D. L. Smith, *J. Vac. Sci. Technol. B* **5**, 1268 (1987).
13. D. H. Chow, R. H. Miles, J. R. Söderström, and T. C. McGill, *Appl. Phys. Lett.* **56**, 1418 (1990).
14. M. J. Cherng, H. R. Jen, C. A. Larsen, G. B. Stringfellow, H. Lundt, and P. C. Taylor, *J. Cryst. Growth* **77**, 408 (1986).
15. N. G. Anderson, Ph.D. thesis, North Carolina State University, Raleigh, 1988.
16. G. D. Pitt, *Contemp. Phys.* **18**, 137 (1977).

2. QUANTUM ELECTRONICS

2.1 Tm:YVO_4 MICROCHIP LASER

Tm:YVO_4 was studied both spectroscopically and as the gain medium in a microchip laser. The crystal had a nominal Tm concentration of 5 at.% and was cut into flat wafers oriented with the crystalline *a*-axis normal to the wafer facets. Absorption measurements, shown in Figure 2-1, are consistent with previous results [1] and show the strongest absorption for 800-nm light polarized along the *c*-axis of the crystal (π polarization). The polarization-resolved fluorescence spectra are presented in Figure 2-2 for wavelengths between 1.6 and 2.0 μm. Time-resolved measurements of the fluorescence indicate a lifetime of 760 μs, independent of wavelength and polarization.

A microchip laser was constructed from a 440-μm-thick wafer of Tm:YVO_4 polished flat and parallel. The crystal was oriented with its *a*-axis parallel to the optic axis of the laser cavity. The pump-side face of the crystal was coated to be highly reflective at all potential lasing frequencies while transmitting > 98% of the pump light (800 nm). The output face reflected the pump light and had a reflectivity of ~ 99.4% for wavelengths between 1.76 and 1.94 μm. Approximately 94% of the incident 800-nm pump light was absorbed by the crystal.

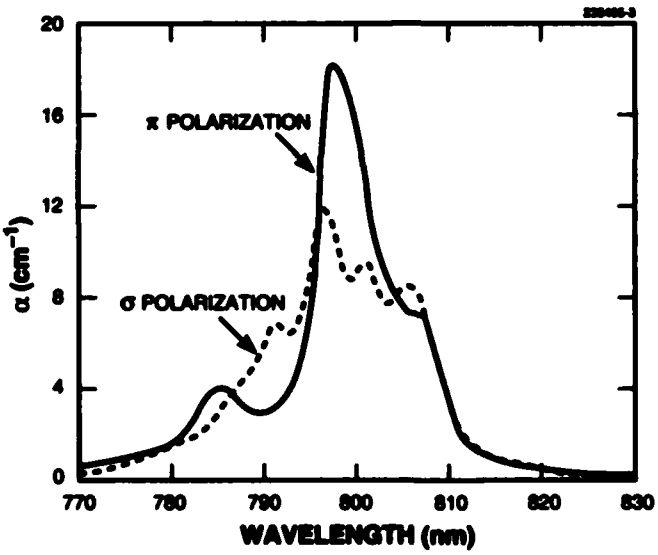

Figure 2-1. Polarization-resolved absorption spectra of Tm:YVO_4 with Tm concentration of 5 at.%.

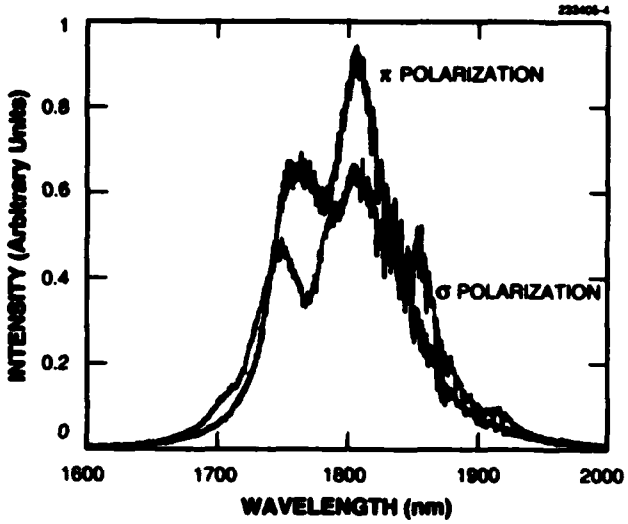

Figure 2-2. Polarization-resolved fluorescence spectra of Tm:YVO_4 with Tm concentration of 5 at.%.

Initially, the Tm:YVO_4 microchip laser was pumped with a Ti:Al_2O_3 laser tuned to 800 nm, in the π polarization, focused to a spot size of ~ 50 μm. The laser oscillated in the σ polarization at 1.94 μm. Input/output data obtained at a crystal temperature of 10°C are shown in Figure 2-3. The threshold incident pump power was ~ 117 mW and the slope efficiency ~ 41%. This is significantly better than previous results reported for Tm:YVO_4 lasers [1], which demonstrated a 370-mW threshold and 25% slope efficiency with respect to the absorbed Ti:Al_2O_3 pump power. The output of the microchip laser had a divergence of < 12 mrad and appeared to be nearly diffraction limited. Spectral measurements indicated that although the laser operated in a single axial mode very close to threshold, five strong axial modes were present at an incident pump power of 218 mW, and more at higher power.

From Figure 2-2, it is seen that the laser emission occurs in the far wing of the fluorescence spectrum. This is, presumably, the result of a large thermal population in the lower laser levels. Given the fact that the fluorescence rises sharply at shorter wavelengths, it was expected that there would be a shift in the oscillating frequency and a significant increase in the laser gain with even modest cooling of the crystal, as is the case with other quasi-three-level lasers. Surprisingly, no measurable change occurred in the lasing frequency or threshold as the crystal temperature was varied between −30 and 20°C. Over the same temperature range, the slope efficiency changed by only 20%.

This microchip laser was also pumped with a 1-W 800-nm diode laser at room temperature. The diode-pumped device had a threshold of ~ 440 mW of incident power and a slope efficiency > 30%, as shown in Figure 2-3. The higher threshold, compared with the same device pumped with a Ti:Al_2O_3 laser,

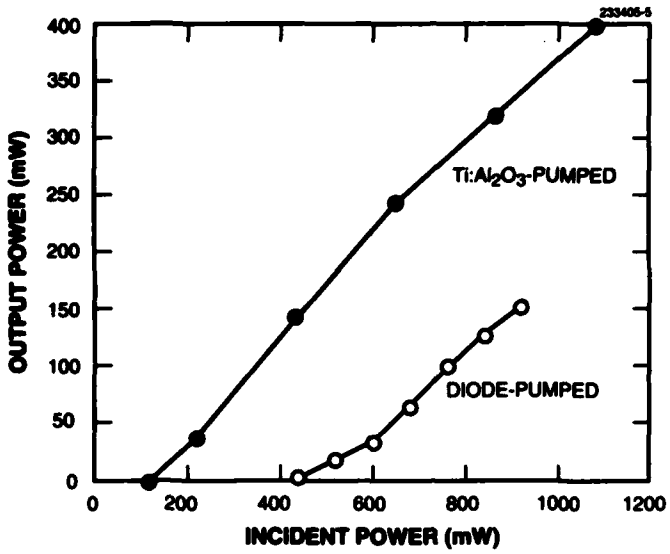

Figure 2-3. Dependence of Tm:YVO_4 microchip laser output power on incident pump power.

is a result of the decreased brightness of the pump source, which results in a larger pumped volume; the slightly lower slope efficiency can be explained by the fact that the crystal was at a higher temperature during the diode-pumped experiment, and was also poorly heat sunk.

The Tm:YVO_4 microchip laser reported here is an efficient room-temperature diode-pumped near-2-μm laser. The output wavelength of the device coincides with a major absorption band in liquid water, which makes it potentially interesting for medical applications.

J. J. Zayhowski
C. Dill III
J. Harrison*
J. R. Ochoa
J. L. Daneu
C. C. Cook

*Author not at Lincoln Laboratory.

2.2 SINGLE-MODE DIODE-PUMPED Nd:YVO_4 MICROCHIP LASER WITH 240 mW OF OUTPUT POWER

A Nd:YVO_4 microchip laser was constructed from a 440-μm-thick wafer of Nd:YVO_4 polished flat and parallel. The crystal, which was oriented with its a-axis parallel to the optic axis of the laser cavity, had a nominal Nd concentration of 0.8 at.% and an absorption coefficient of 23 cm^{-1} for π-polarized light at 809 nm. The pump-side face of the crystal was coated to be highly reflective at the lasing wavelength (1.064 μm) while transmitting ~ 98% of the pump light (800 nm). The output face had a reflectivity of ~ 60% for the lasing wavelength and 25% for the pump. As a result of the short crystal length and the low pump reflectivity of the output face, only 70% of the incident pump light was absorbed by the gain medium. Nevertheless, an output power of 240 mW was obtained for 940 mW of incident diode pump power.

The Nd:YVO_4 microchip laser was pumped with the focused output of a 1-W diode laser. When the spot size of the pump was adjusted to maximize the output power of the microchip laser, it oscillated in a double-lobed far-field pattern at high powers. It was possible, however, to obtain single-lobed, near-diffraction-limited performance at all power levels with only a small sacrifice in output power (< 10% at the highest pump power); the transition from a double-lobed to a single-lobed far-field pattern was abrupt. The focusing was therefore adjusted to obtain the maximum near-diffraction-limited power at the highest pump levels and was left fixed for all measurements. The dependence of the Nd:YVO_4 microchip laser output power on the incident pump power under the pump conditions just described is shown in Figure 2-4. The nonlinear shape of the input/output curve is a result of the changing radius of the lasing mode as a function of pump power [2].

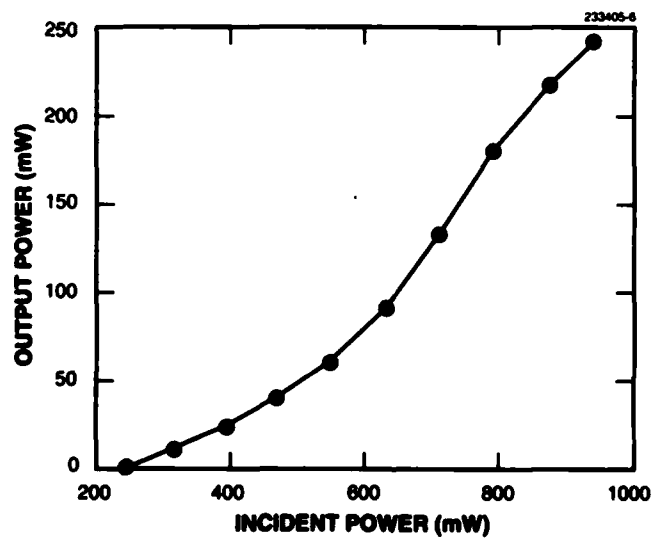

Figure 2-4. Dependence of Nd:YVO_4 microchip laser output power on incident pump power.

A 1/4-m spectrometer was used to monitor the output wavelength of the microchip laser. Oscillation occurred at a single frequency, 1.064 μm, at all output powers. Although this is not surprising in light of previous results [3]–[6], it does represent the highest-power single-frequency microchip laser yet reported.

J. J. Zayhowski J. L. Daneu
C. Dill III C. C. Cook

2.3 APERTURE GUIDING IN QUASI-THREE-LEVEL LASERS

In end-pumped Nd^{+3} microchip lasers with flat-flat cavities, thermal guiding has been demonstrated to be the predominant mechanism that stabilizes the laser cavity though either a change of refractive index with temperature [7] or a thermally induced bulge on the mirror surface [8]. Diode-pumped Yb:YAG lasers at 1.03 μm have been demonstrated recently [9], and these have the attractive features relative to Nd:YAG of longer upper-state lifetime, larger absorption bandwidth, and lower heat dissipation. The heat dissipated per unit pump power in Nd:YAG is three to four times larger than in Yb:YAG because of the low quantum defect in Yb:YAG, which has a pump wavelength of 0.94 μm and a lasing wavelength of 1.03 μm. If thermal guiding is the predominant mechanism for stabilizing the cavity mode in Yb:YAG, then the predicted spot size and laser threshold power are relatively large because of the low heat dissipation. In practice, we observe much smaller spot size and threshold power than predicted by thermal guiding alone. When aperture guiding is modeled, we obtain good agreement between the experimental results and the model. All end-pumped, quasi-three-level lasers are self-aperturing; in the unpumped regions, absorption occurs at the laser wavelength because of population in the lower laser level, while gain occurs in the pumped regions.

A schematic of the diode-pumped Yb:YAG laser experiment is shown in Figure 2-5. The laser gain element had 25-at.% Yb doping and was 400 μm thick with flat polished faces. The two end faces were dielectrically coated, with one having a dichroic coating with high reflectivity at 1.03 μm and 95% transmission at 0.94 μm, and the other having 98% reflectivity at 1.03 μm. The Yb:YAG laser was pumped with two InGaAs diode lasers operating at 0.94 μm. Each diode laser was collimated in the plane perpendicular to the junction by a gradient index lens and then collimated by a cylindrical lens in the plane of the junction. The beams were then focused into the gain element by a 2.5-cm focal length lens in a geometric multiplexed configuration. The equivalent Gaussian beam radii at the gain element were 43 μm in the vertical plane and 47 μm in the horizontal plane.

Figure 2-6 shows the output power and cavity mode radius as a function of the absorbed pump power. The slope efficiency was 47% relative to absorbed power (fitted to the four highest-power data points). The radius was 42 μm for 30-mW output power and decreased to 35 μm at the highest output power. The M^2 in both planes was measured to be < 1.05 at all power levels.

The measured cavity mode radius is significantly smaller than predicted by thermal guiding alone. If the results of Zayhowski [7] for Nd:YAG microchip lasers are scaled to this Yb:YAG laser experiment, then the estimated cavity mode radius for the Yb:YAG laser pumped with 0.5 W of power is ~ 120 μm. The calculated threshold power for this mode radius is ~ 0.5 W, and thus the observed results are in substantial disagreement with the thermal guiding prediction.

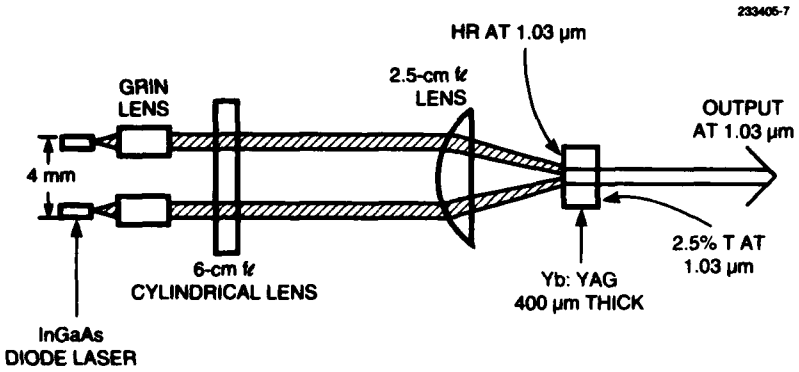

Figure 2-5. Schematic of Yb:YAG microchip laser experiment viewed in plane perpendicular to InGaAs diode laser junctions. The cylindrical lens collimates the light in the plane of the junction.

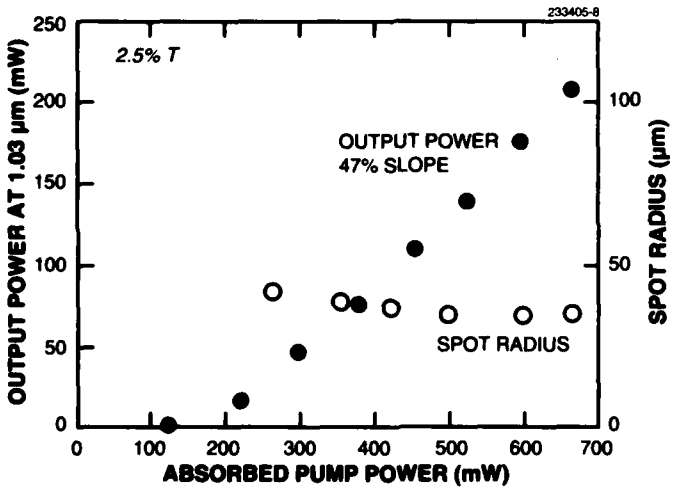

Figure 2-6. Yb:YAG microchip laser output power and cavity mode radius as a function of incident pump power.

This discrepancy, we believe, is explained by aperture guiding. We have modeled the effect of aperture guiding by numerical modeling of the (in general) non-Gaussian laser mode using the fast Fourier transform method. In these calculations we have ignored any effects due to thermal guiding or gain saturation, and thus the results are valid only near laser threshold.

We have modeled the pump beam by allowing its intensity profile to be super-Gaussian of varying order with

$$I(r) = I_0 \exp\left[2\left(r / w_p\right)^n\right] . \tag{2.1}$$

Here, $I(r)$ is the intensity of the pump beam as a function of radius, w_p is the super-Gaussian beam radius, and n is the super-Gaussian order where n is even.

The cavity is modeled as two flat reflector mirrors with an intracavity aperture placed in the plane of the high reflector with varying super-Gaussian order (n = 2, 4, 6, and 8), and the transverse profile of the output beam is calculated. The results from the numerical calculations for each super-Gaussian order are shown in Table 2-1. The predicted output beams are essentially Gaussian in intensity for all orders of super-Gaussian aperture, and the cavity mode radii are derived from least-square fits of Gaussians to the output beam profile. The fact that even high-order super-Gaussian pump profiles yield Gaussian intensity output beams is not surprising for low Fresnel number cavities; hard-edge intracavity apertures (essentially $n = \infty$) with low Fresnel number are often used to select the Gaussian TEM_{00} mode in lasers.

TABLE 2-1

Cavity Mode Radius Predictions from Fast Fourier Transform Calculations

Super-Gaussian Order (n)	Cavity Mode Radius (μm)
2	45
4	44
6	44
8	43

The modeled cavity mode radii are largely insensitive to the super-Gaussian order of the aperture transmission, which suggests that the main determinant of the cavity mode radius is the pump power within a given area as opposed to the exact transverse dependence of the pump intensity. The modeled cavity mode radii are in good agreement with the measured cavity mode radius near threshold, showing that aperture guiding is indeed the dominant mechanism in determining the cavity mode radius in this laser.

T. Y. Fan

REFERENCES

1. H. Saito, S. Chaddha, R. S. F. Chang, and N. Djeu, *Opt. Lett.* **17**, 189 (1992).
2. J. J. Zayhowski, *OSA Proc. Advanced Solid-State Lasers* **6**, 9 (1991).
3. J. J. Zayhowski, *Opt. Lett.* **15**, 431 (1990).
4. G. J. Kintz and T. Baer, *IEEE J. Quantum Electron.* **26**, 1457 (1990).
5. T. Sasaki, T. Kojima, A. Yokotani, O. Oguri, and S. Nakai, *Opt. Lett.* **16**, 1665 (1991).
6. T. Taira, A. Mukai, Y. Nozawa, and T. Kobayashi, *Opt. Lett.* **16**, 1955 (1991).
7. J. J. Zayhowski, *Lincoln Lab. J.* **3**, 427 (1990).
8. P. A. Leilabady, D. W. Anthon, and P. O. Gullicksen, in *Conference on Lasers and Electro-Optics, 1992 Technical Digest Series*, Vol. 12 (Optical Society of America, Washington, D.C. 1992), p. 54.
9. P. Lacovara, H. K. Choi, C. A. Wang, R. L. Aggarwal, and T. Y. Fan, *Opt. Lett.* **16**, 1089 (1991).

3. MATERIALS RESEARCH

3.1 HIGH-POWER GaInAsSb/AlGaAsSb MULTIPLE-QUANTUM-WELL DIODE LASERS EMITTING AT 1.9 μm

High-power diode lasers emitting at ~ 1.9 μm have many potential applications such as in pumping Ho-doped solid state lasers emitting at 2.1 μm, and in tissue welding and surgery because of strong absorption in human tissue. Diode lasers incorporating GaInAsSb active layers and AlGaAsSb confining layers grown on GaSb substrates have the potential for emission in the 1.7–5-μm spectral range. Recently, the performance of such lasers emitting at ~ 2 μm has shown significant improvements by incorporating a multiple-quantum-well active region consisting of GaInAsSb wells and AlGaAsSb barrier layers [1],[2]. Room-temperature pulsed threshold current density as low as 260 A/cm^2, differential quantum efficiency as high as 70%, and single-ended CW output power as high as 600 mW/facet have been demonstrated. Here, we report high-performance GaInAsSb/AlGaAsSb diode lasers emitting at ~ 1.9 μm with room-temperature threshold current density as low as 143 A/cm^2 and single-ended CW output power as high 1.3 W at a heatsink temperature of 12°C. The improvement in the performance is a result of more optimized growth conditions.

To prepare a wafer for laser fabrication, the following layers were grown on an n-GaSb substrate by molecular beam epitaxy: n^+-GaSb buffer, 2-μm-thick n-$Al_{0.85}Ga_{0.15}As_{0.07}Sb_{0.93}$ cladding, active region consisting of five 10-nm-thick $Ga_{1-x}In_xAs_ySb_{1-y}$ wells and six 20-nm-thick $Al_{0.25}Ga_{0.75}As_{0.02}Sb_{0.98}$ barriers, 2-μm-thick p-$Al_{0.85}Ga_{0.15}As_{0.07}Sb_{0.93}$ cladding, and 0.05-μm-thick p^+-GaSb contacting. All the layers are nominally lattice matched to the substrate, except for the active wells, which are under compressive strain of ~ 5×10^{-3} as determined by double-crystal x-ray diffractometry. Based on the growth parameters and the amount of strain, the best estimate for the active layer composition is $x = 0.14$ and $y = 0.05$. The compressive strain was found to reduce the threshold current density substantially because it reduces the density of states for the valence band and increases the valence-band offset between the active and the barrier layers. The valence-band offset between the active and barrier layers for the above laser structure is calculated to be ~ 90 meV, while the conduction-band offset is ~ 350 meV.

To characterize the quality of the laser structure, broad-stripe devices 300 μm wide were fabricated using the lift-off process. Figure 3-1 shows the room-temperature pulsed threshold current density J_{th} vs inverse cavity length L^{-1}. For L = 2 mm, J_{th} = 143 A/cm^2, which is much smaller than 260 A/cm^2 reported previously for a similar laser structure with emission wavelength at ~ 2.1 μm [1]. As L becomes smaller, the value of J_{th} increases gradually, to a value of 280 A/cm^2 for 300 μm. The gain coefficient, which is inversely proportional to the slope, is much larger for these lasers than for the ones reported previously.

Figure 3-2 shows J_{th} vs heatsink temperature for pulsed operation of a 1000-μm-long laser. Near room temperature, the characteristic temperature T_0 is 95 K, which is significantly higher than 55 K obtained for InGaAs/InP lasers emitting at ~ 2 μm [3]. The value of T_0 decreases to ~ 70 K at 70°C. For GaInAsSb/AlGaAsSb quantum-well lasers emitting at ~ 2.1 μm, a characteristic temperature as high as 113 K has been obtained [1].

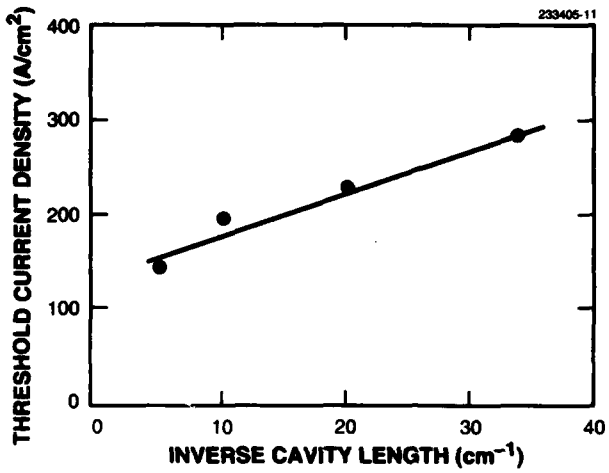

Figure 3-1. Room-temperature pulsed threshold current density vs inverse cavity length for 300-μm-wide GaInAsSb/AlGaAsSb quantum-well lasers.

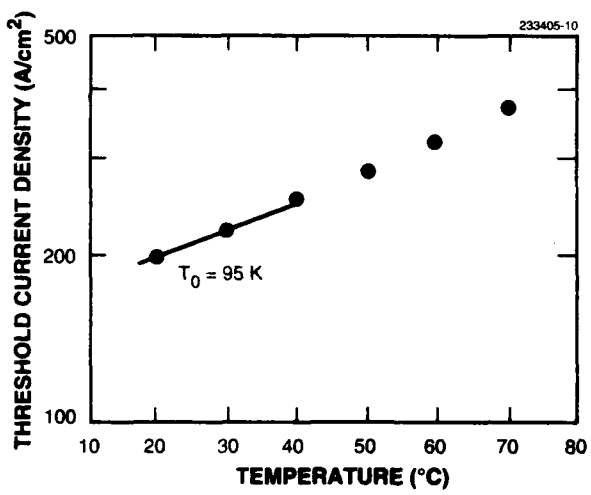

Figure 3-2. Pulsed threshold current density vs heatsink temperature for quantum-well GaInAsSb/AlGaAsSb laser 1000 μm long.

Lasers with a silicon-dioxide-defined stripe 300 μm wide were fabricated for CW operation. The front and back facets were coated to have reflectivities of 4 and 95%, respectively. Several devices 1000 μm long were mounted junction-side down on copper heatsinks using In solder. Figure 3-3 shows the output power vs current for a device operated at a heatsink temperature of 12°C. The threshold current is ~ 650 mA and the initial slope efficiency is ~ 0.3 W/A, corresponding to a differential quantum efficiency of 47%. The maximum output power is 1.3 W, limited by the junction temperature rise. The power conversion efficiency is as high as 15.5%. A preliminary reliability test of these lasers is very encouraging. One device operated at 700 mW has not shown any degradation for 500 h. All other devices operated for shorter periods have exhibited stable operation.

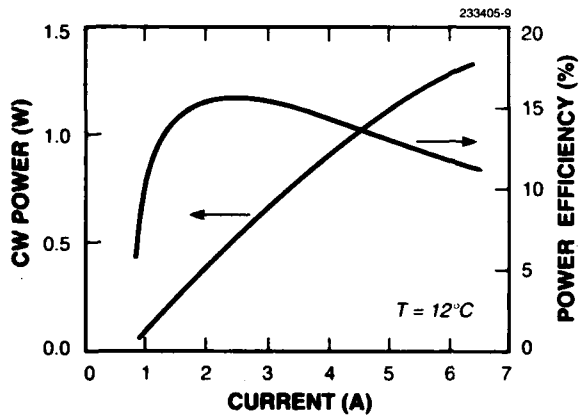

Figure 3-3. Output power vs current for CW operation of 300-μm-wide by 1000-μm-long GaInAsSb/AlGaAsSb quantum-well laser.

The emission spectra of the laser show multiple longitudinal modes at ~ 1.92 μm. The full width at half-maximum of the spectrum is ~ 4 nm at low power levels but increases gradually to ~ 7 nm at a power level of 1 W. The longitudinal mode spacing for L = 1 mm is ~ 0.5 nm. The peak wavelength under CW conditions increases with increasing heatsink temperature at a rate of 1.2 nm/°C.

H. K. Choi
G. W. Turner
S. J. Eglash

3.2 GROWTH OF UNDOPED AND Se-DOPED GaSb BY ORGANOMETALLIC VAPOR PHASE EPITAXY

GaSb and its related ternary and quaternary alloys are of interest for a variety of optoelectronic devices operating in the range 2–5 μm. Here, we report the growth and electrical characteristics of undoped and Se-doped GaSb grown on GaAs substrates by low-pressure organometallic vapor phase epitaxy (OMVPE).

The GaSb epilayers were grown in a vertical rotating-disk (250 rpm) OMVPE reactor operated at 0.2 atm. The source materials were trimethylgallium (TMGa), trimethylantimony (TMSb), and 100% arsine. The carrier gas was H_2 at a flow rate of 10 slpm. The TMGa mole fraction was held constant at 3×10^{-4}, while the TMSb mole fraction ranged from 1.8 to 3.3×10^{-4}, which resulted in a range of V/III ratios between 0.6 and 1.1. The *n*-type doping of GaSb was studied using 500-ppm H_2Se diluted in H_2. The GaSb growth temperature was varied from 560 to 640°C.

Epilayers of GaSb were grown on semi-insulating (001) GaAs substrates oriented 2° toward [110]. First, a 40-nm-thick GaAs buffer layer was grown at 680°C. The wafer was then cooled under an arsine flow to the growth temperature used for GaSb. The surface morphology of GaSb layers was examined by Nomarski contrast microscopy. The thickness of GaSb layers was measured by cleaving the sample and stain etching to reveal the epilayer-substrate interface. Electrical characterization was performed using Hall measurements.

The dependence of GaSb growth rate on temperature was studied for a constant V/III ratio of 1. The rate, normalized to TMGa mole fraction, is shown as a function of inverse temperature in Figure 3-4. Growth is kinetically limited for the entire temperature range investigated between 560 and 640°C. The activation energy for growth is 20.4 kcal/mol, which is significantly lower than the value of 36 kcal/mol reported previously for growth at atmospheric pressure [4].

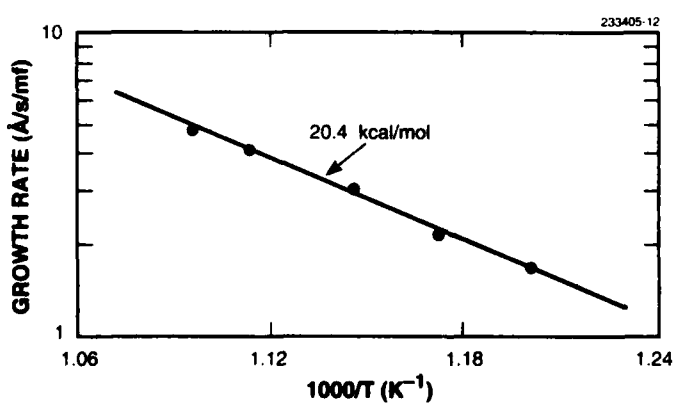

Figure 3-4. GaSb growth rate dependence on inverse growth temperature.

The surface morphology of GaSb layers grown at a temperature of 600°C and a V/III ratio of 0.7–1.0 is shown in Figure 3-5. A textured but otherwise featureless mirror morphology was obtained only for layers grown with V/III = 0.8. For layers grown with V/III = 0.7, the surface was hazy to the eye. Auger analysis indicated that the surface was Ga-rich with areas of pure Ga. For layers grown with V/III ≥ 0.9, faceted defects were observed that were analyzed to be stoichiometric GaSb. The defect size increased with V/III. The V/III ratio for optimum morphology at this temperature as well as over the temperatures studied is in an extremely narrow range, but a mirror morphology could be obtained by adjusting the V/III ratio. Accordingly, Figure 3-6 shows the V/III ratio for various growth temperatures that resulted in a defect-free, stoichiometric mirror surface morphology. Below the indicated line the surface was Ga-rich, while above the line the surface contained faceted defects.

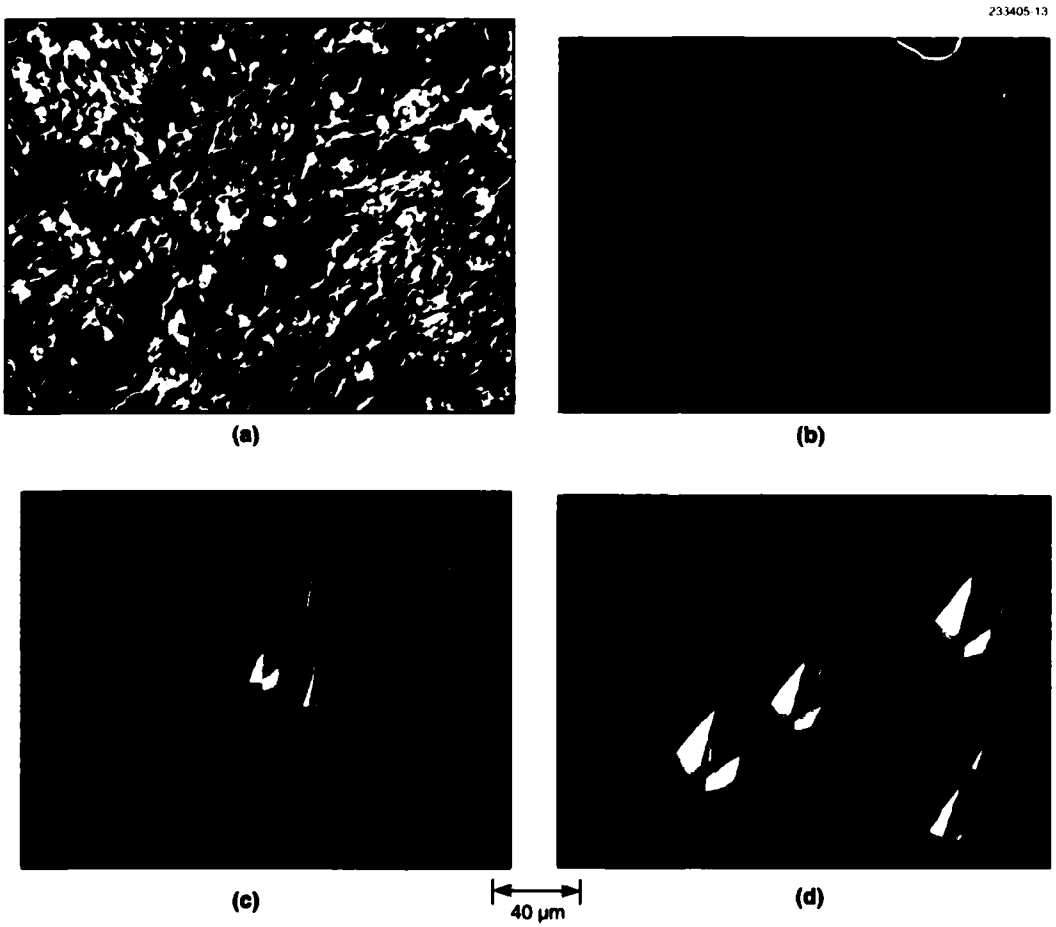

Figure 3-5. Surface morphology of GaSb layers grown on GaAs substrates at 600°C and with V/III ratios of (a) 0.7, (b) 0.8, (c) 0.9, and (d) 1.0.

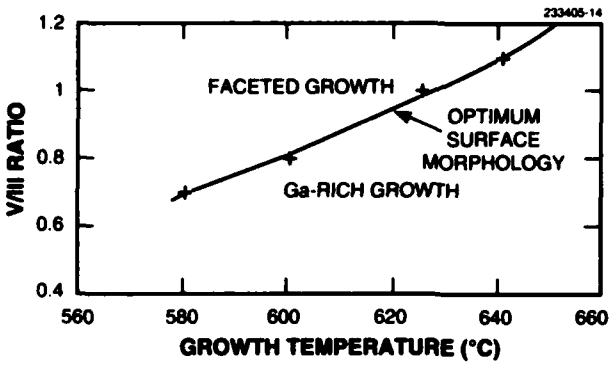

Figure 3-6. V/III ratio vs growth temperature for optimum surface morphology of GaSb layers grown on GaAs substrates.

The electrical properties of epilayers grown on mismatched substrates are commonly influenced by defects generated at the substrate-epilayer interface. For GaSb layers grown at 600°C, Hall data indicated that for ≥ 3-μm layer thickness, the electrical characteristics were dominated by the bulk layer. Therefore, all electrical measurements reported are for layers at least 3 μm thick. The effect of growth temperature on the electrical properties measured at 77 K is shown in Figure 3-7 for epilayers grown at temperatures from 580 to 640°C. Over this range, the V/III ratio was varied as indicated in Figure 3-6 to yield the optimum morphology. The layers were always *p*-type as is typically observed for epitaxially grown GaSb [5]. The lowest hole concentration was 1.1×10^{16} cm^{-3} with corresponding hole mobility of 3.8×10^3 cm^2/V s, which was obtained for layers grown at 580°C. For layers grown at temperatures of 600 and 625°C, the hole concentration and mobility were nearly constant at ~ 2.2×10^{16} cm^{-3} and 2.7×10^3 cm^2/V s, respectively. A slight decrease in hole mobility to 2.5×10^3 cm^2/V s was measured for the layer grown at 640°C.

The *n*-type doping of GaSb layers was studied using H_2Se at a mole fraction from 2.5 to 10×10^{-7} and growth temperatures between 580 and 640°C. Layers were grown with the V/III ratio adjusted appropriately to achieve a defect-free surface morphology. In general, the electron concentration initially increases with H_2Se mole fraction and then saturates, while the corresponding mobility continually decreases, in agreement with previously reported results [6]. For the low growth temperature of 580°C and lowest H_2Se mole fraction, the electron concentration was already at a saturated level. With increasing growth temperature, the H_2Se mole fraction at which the electron concentration saturated increases, but the maximum concentration level attainable decreases. The data in Figure 3-8 for layers grown with H_2Se mole fraction of 2.5×10^{-7} show that the electron concentration measured at 77 K decreases from 4.9×10^{17} cm^{-3} at 580°C to 1.9×10^{17} cm^{-3} at 640°C, with a corresponding increase in mobility from 1.5 to 2.1×10^3 cm^2/V s. The highest electron concentration was 4.9×10^{17} cm^{-3} with a corresponding electron mobility of 1.5×10^3 cm^2/V s for growth at 580°C.

C. A. Wang
J. H. Reinold

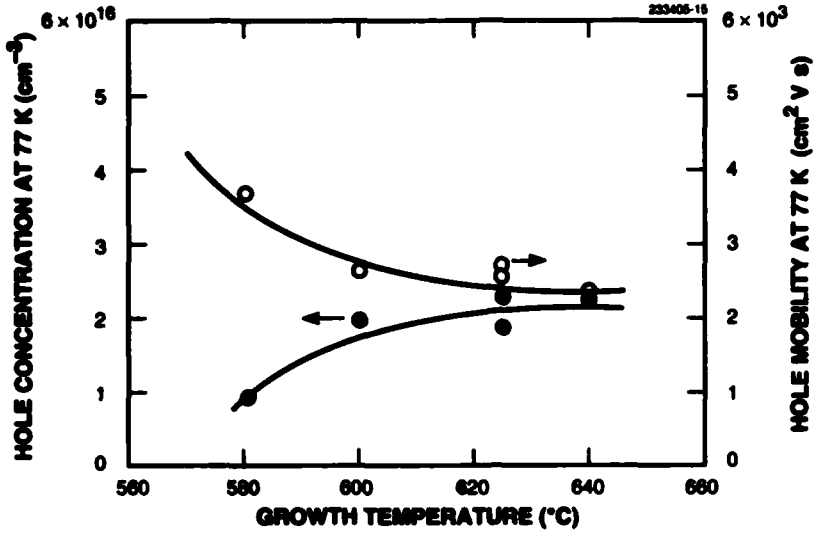

Figure 3-7. Hole concentration and mobility at 77 K for undoped GaSb layers as a function of growth temperature.

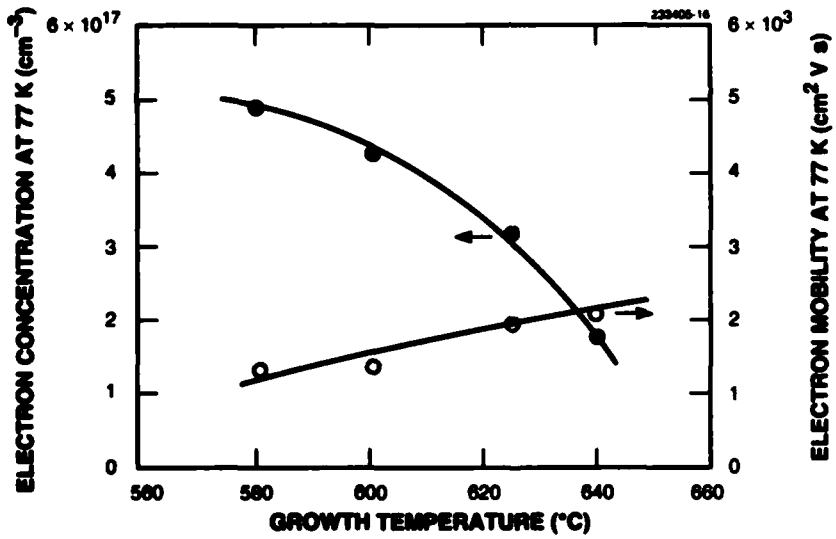

Figure 3-8. Electron concentration and mobility at 77 K for Se-doped GaSb layers as a function of growth temperature.

REFERENCES

1. H. K. Choi and S. J. Eglash, *Appl. Phys. Lett.* **61**, 1154 (1992).
2. S. J. Eglash and H. K. Choi, presented at IEEE Lasers and Electro-Optics Society Annual Meeting, Boston, Mass., 16–19 November 1992, Paper DLTA 8.3.
3. J. S. Major, Jr., D. W. Nam, J. S. Osinski, and D. F. Welch, *IEEE Photon. Technol. Lett.* **5**, 594 (1993).
4. F. Pascal, F. Delannoy, N. Bougnot, L. Gouskov, G. Bougnot, P. Grosse, and J. Kaoukab, *J. Electron. Mater.* **19**, 187 (1990).
5. A. G. Milnes and A. Y. Polykakov, *Solid-State Electron.* **36**, 803 (1993).
6. F. Nakamura, K. Taira, K. Funato and H. Kawai, *J. Cryst. Growth* **115**, 474 (1991).

4. SUBMICROMETER TECHNOLOGY

4.1 MOSAIC DIAMOND SUBSTRATES APPROACHING SINGLE-CRYSTAL QUALITY USING CUBE-SHAPED DIAMOND SEEDS

Two techniques are being developed to obtain electronic-grade single-crystal diamond substrates. One uses heteroepitaxy to grow diamond films on a foreign single-crystal substrate, like Si [1],[2] or Ni [3]–[5]. Although the foreign substrate is single crystal, the overlayer diamond films are mosaic, that is, they consist of many small crystals whose orientations vary a few degrees from an average orientation. The smallest angular deviation yet obtained [6] is approximately ± 2.5°, but this is expected to improve with additional development as the films approach single-crystal quality. The other technique uses existing small single subcrystals that are oriented to form a larger mosaic structure, on which a small amount of diamond is homoepitaxially grown to form a continuous substrate. The quality of the substrate depends both upon the characteristics of the small starting subcrystals and the consistency of the crystallographic orientation. Tetrahedron- or cube-shaped diamonds produced commercially in high-pressure diamond presses can be used as subcrystals in the mosaic process. They cost from one to ten dollars a carat, which is about an order of magnitude less than diamond grown by chemical vapor deposition.

Here, we discuss the use of cube-shaped diamond subcrystals, shown in Figure 4-1, to obtain large-area substrates that require only 20 μm of homoepitaxial diamond growth. Unlike tetrahedron-shaped crystals which are oriented with lithographically defined tetrahedral matching pits, cubic subcrystals are difficult to orient with either cubic pits or square profile gratings. However, as suggested by Yoder [7], faceted crystals may be oriented one to another by surface tension of a liquid that wets the subcrystals.

The diamond cubes are cleaned in a 150°C solution of H_2O_2 and H_2SO_4, and rinsed in water, acetone, and finally isopropyl alcohol. They are then placed on a smooth substrate, like a polished Si wafer, and fused together by wetting both the diamonds and substrate with a solution of glycerin and isopropyl alcohol. The mixture, consisting of nearly equal parts by volume, is adjusted to obtain the desired viscosity. With this technique, several hundred cubes coalesce to form structures of 20–30 cubes, about 4–6 cubes on a side. All the cubes within the same structure have the same crystal orientation to within a few tenths of a degree as determined by the alignment of the square (100) facets of the cubes. However, the structures are randomly oriented with respect to each other. A junction between two adjacent structures is shown in Figure 4-2.

Consistent orientation between the coalesced structures can be achieved using a square frame composed of ~ 1-mm-high vertical walls on the supporting substrate. With a metal probe and the aid of a low-power microscope, the coalesced structures are pushed inside the frame where they become oriented to the vertical walls. When using cubes ~ 250 μm on a side and a frame with an ~ 0.5-cm-wide opening, a square region 0.5 cm on a side can be filled with oriented diamond cubes within 30 min, depending upon the experience of the operator. Figure 4-3 shows a typical in-plane angular variation of the cube after orientation with a square frame (solid circles), with a standard deviation of 1.7°. The areas with the largest in-plane angular deviation correspond with cubes that were either significantly larger or smaller than average.

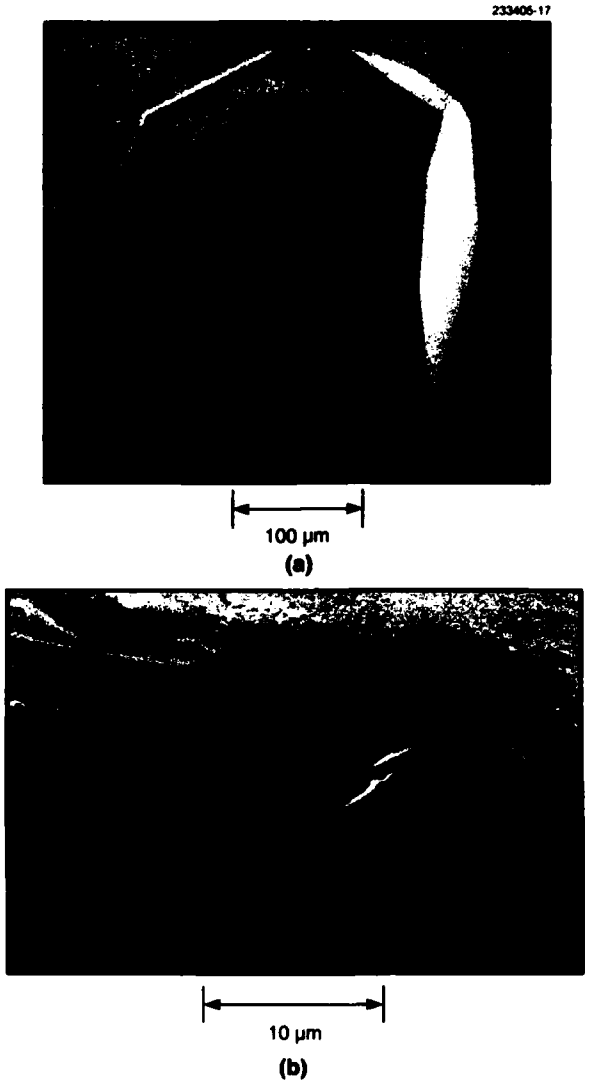

Figure 4-1. (a) Scanning electron micrograph (SEM) of a cubic diamond; the square faces of the cube are (100) planes and the corners are faced with (111) planes. (b) Higher-magnification SEM of the top right corner of the crystal in (a).

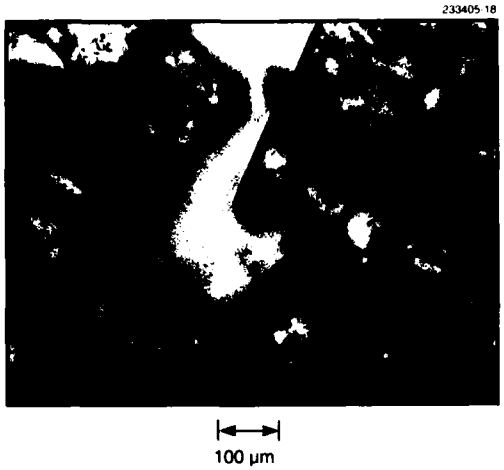

Figure 4-2. Optical micrograph of junction of two coalesced structures with different crystal orientations.

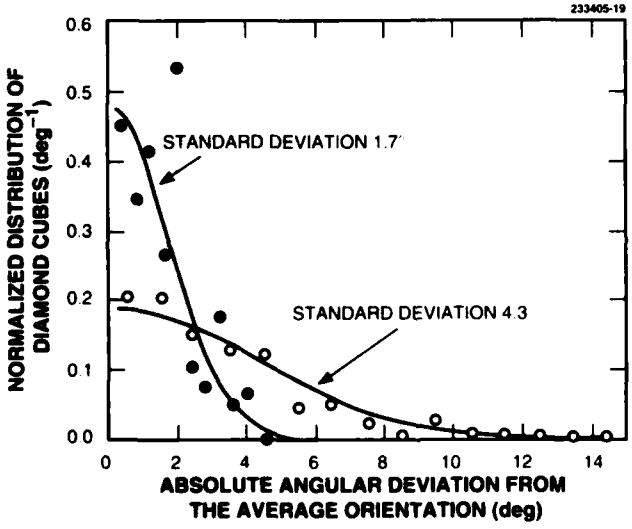

Figure 4-3. Distribution of in-plane orientation of diamond cubes after orientation with square frame (solid circles) and by pushing and deforming layer of cubes (open circles).

The excessive time required to orient the structures has led to the development of faster techniques. One successful way to align the randomly oriented regions is to push from the side on the layer of cubes with metal probes. This causes the structures of coalesced subcrystals to deform and realign to a common orientation. Initially, the layer of cubes is shaped into an approximate square. With the use of an ~ 100-μm-diam probe, one of the corners of the square is pushed in until the cubes in the center of the square are displaced ~ 200 μm, and then the remaining corners are pushed in. After the four corners are pushed in, the layer of cubes is reformed into the shape of a square by using the straight edge of a microscope slide. A sequence of four iterations of this procedure causes the central region of the layer of cubes to become consistently oriented. Figure 4-3 shows the distribution of the orientation of cubes after using this pushing technique (open circles), with a standard deviation of 4.3°. Again, the largest angular deviation of the cubes corresponded with cubes either significantly larger or smaller than average. The limitation on the degree of orientation appears to be the distribution of cube size, which is ~ 250 μm on a side with a standard deviation of 20 μm.

If all cubes were the same size, the in-plane orientation would be limited by the smoothness of the facets of the cubes. As seen from Figure 4-1, the cubes have steps of a few micrometers on their (100) facets, resulting in a minimum variation of in-plane orientation of a few tenths of a degree. This variation is consistent with the results in Figure 4-4, showing the distribution of angles between the substrate surface and the plane of the cubes contacting the surface.

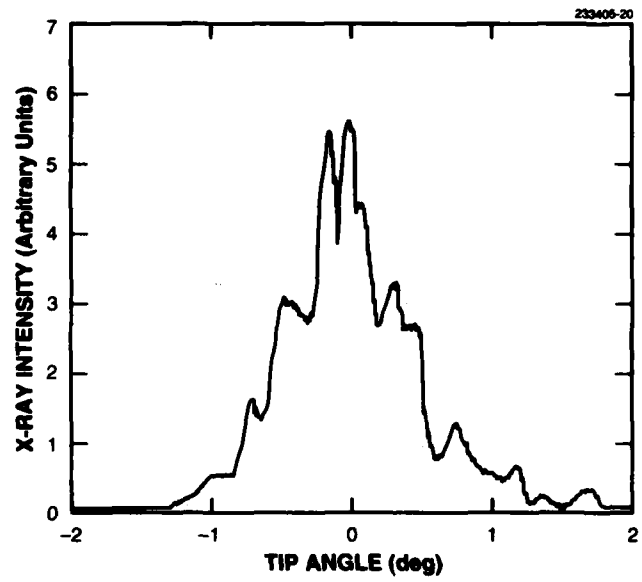

Figure 4-4. Distribution of tip angles between (100) planes and substrate surface as determined by x-ray diffraction.

Once the diamond cubes are oriented, the glycerin is evaporated by heating, the diamond cubes are glued in place with a novolac-based polymer, and then an oxygen plasma is used to remove the excess polymer from the diamonds prior to homoepitaxial growth [8]. After ~ 20 μm of homoepitaxial diamond growth the individual diamonds have coalesced to form a continuous substrate. Upon examining cleaved substrates, < 10 μm of the common surface between the diamond cubes has fused together. It is expected that by changing the diamond growth conditions, more of the common surface between adjacent diamond cubes will coalesce. We have found that care must be taken in initiating homoepitaxial growth on synthetic diamond, or else twinned crystals will also be seeded from the synthetic diamond. These twinned regions are often difficult to cover with additional defect-free homoepitaxial diamond.

M. W. Geis
N. N. Efremow, Jr.
R. Susalka
J. C. Twichell
K. A. Snail*
C. Spiro*
B. Sweeting*

4.2 RESONANT-TUNNELING TRANSMISSION LINES

The application of quantum-effect devices in digital circuits is presently of great interest for computing and signal processing. The central principle of these devices is multistable operation by use of negative differential resistance (NDR). This report describes a bistable quantum-effect device consisting of resonant-tunneling structures monolithically integrated with high-frequency transmission lines as a basis for digital logic and waveforming applications. The key advantage of the resonant-tunneling structure over conventional circuit approaches is that the nonlinear switching elements couple directly to a quasi-TEM mode of the transmission line. This greatly reduces the deleterious effects of interconnects, which have high capacitance and therefore can easily limit the speed of quantum-effect devices in a conventional circuit.

Figure 4-5 illustrates how bistability is achieved in the present device. Figure 4-5(a) shows a configuration of a resonant-tunneling diode (RTD) and a load resistor. In Figure 4-5(b) we see that the load line intersects the RTD current-voltage (I-V) curve at three points; the two where the RTD has a positive differential resistance (I and III) are unconditionally stable, while the one in the NDR region (II) is ac unstable. For ease of monolithic integration a bistable circuit made only of RTDs is desirable. One such configuration, shown in Figure 4-5(c), utilizes two RTDs of different areas, a large one as the switching element and a small one as the load resistor. The theoretical I-V curve for a 2:1 ratio of the areas is shown in Figure 4-5(d).

*Author not at Lincoln Laboratory.

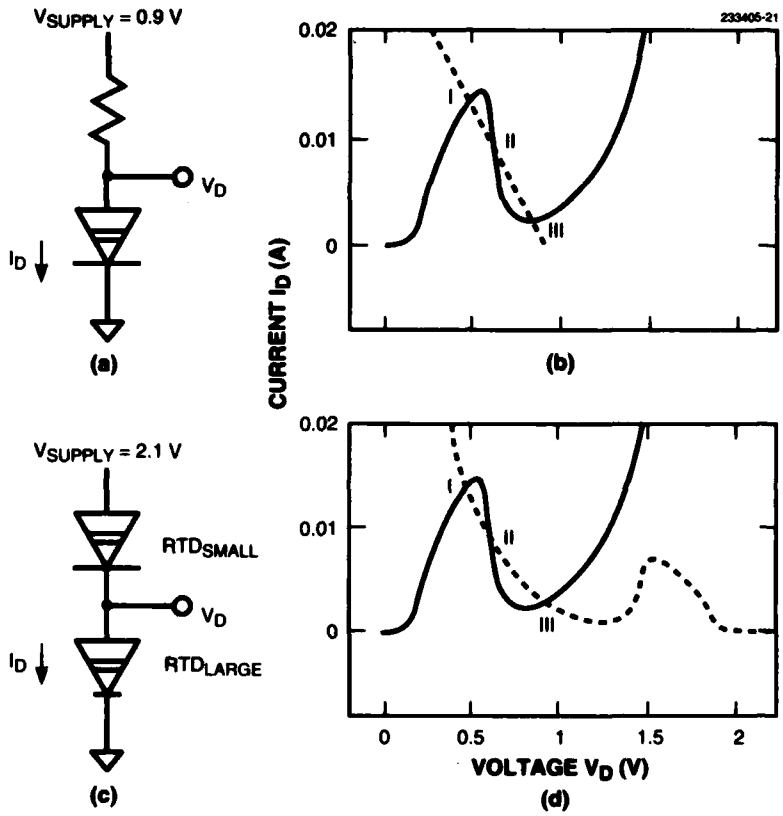

Figure 4-5. Resonant-tunneling diode (RTD) circuits demonstrating bistable operation. (a) Diagram and (b) current-voltage (I-V) characteristic for RTD with resistive load. (c) Diagram and (d) I-V characteristic for RTD with smaller RTD load. In (b) and (d) the dashed lines indicate load lines. For both (b) and (d) the intersections of the load lines with the device characteristics determine the possible operating points (labeled I, II, and III) for the circuits.

The bistable RTD circuit can be integrated with a transmission line to form a bistable transmission line, shown in Figure 4-6, which could be used in high-speed digital applications as a low-loss interconnect or for pulse-shaping applications. A ten-stage bistable lossy transmission line has been simulated using the SPICE 3e computer program. Figure 4-7 shows a typical result in which a 5-GHz sine wave is transformed into a square wave of the same period and comparable amplitude after passing through the transmission line. The small blips during the last cycle are attributed to reflections that occur between adjacent RTD sections.

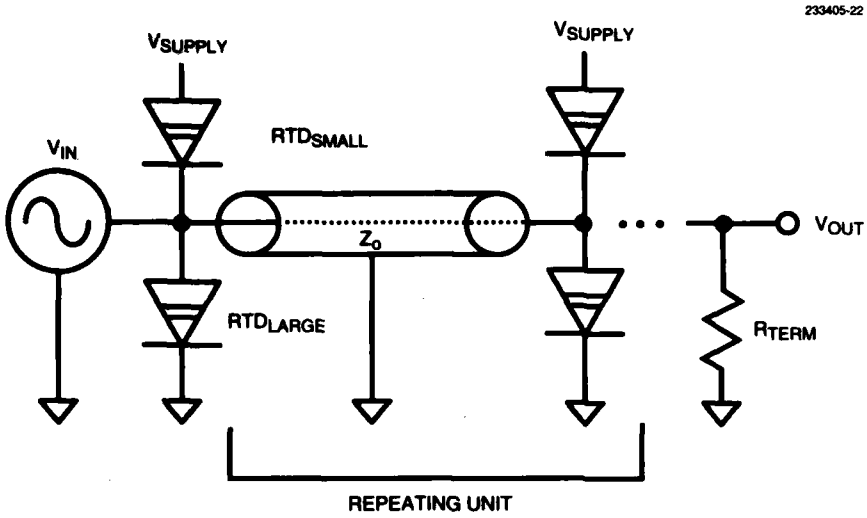

Figure 4-6. Bistable transmission line suitable for logic interconnect or pulse shaping.

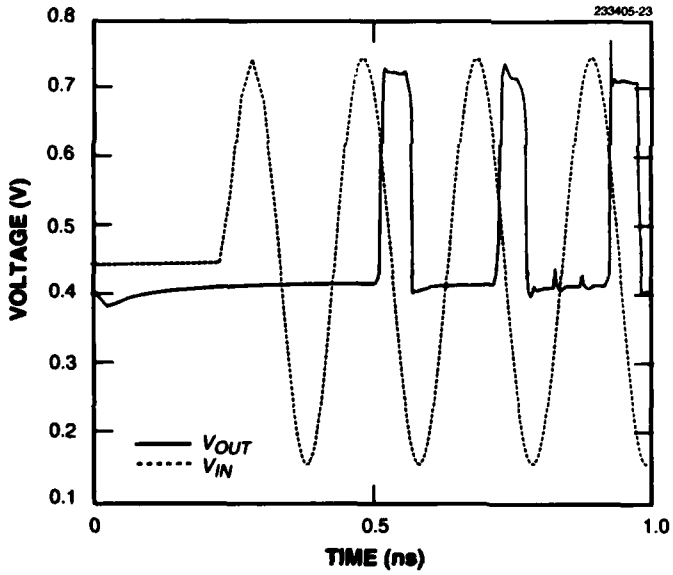

Figure 4-7. Computer simulation of ten-stage bistable transmission-line structure showing pulse shaping. In this simulation $Z_0 = 50\ \Omega$ and $R_{term} = 50\ \Omega$. The effective propagation velocity is 8.3×10^9 cm s^{-1}, the series resistive loss is $2.4 \times 10^2\ \Omega\ cm^{-1}$, and the length of each segment is 0.2 cm.

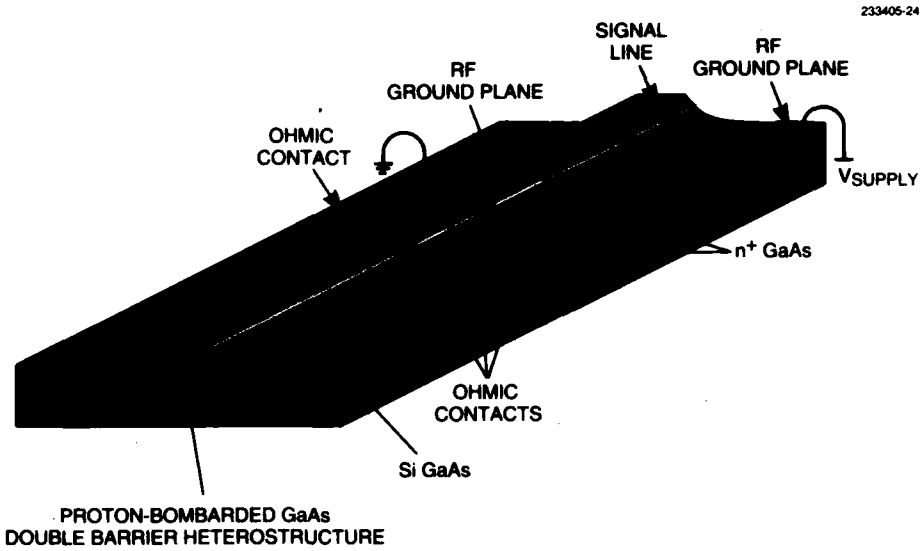

Figure 4-8. Sketch of proposed implementation of RTD transmission line.

The physical implementation of the proposed circuit in the GaAs/AlGaAs materials system is shown in Figure 4-8. The RTDs are defined vertically with a double-barrier heterostructure whose total thickness is ~ 10 nm. The ground plane of the transmission line also provides bias to the load and switching elements of the circuit. Current flows to the RTDs through channels of n^+ GaAs, so ohmic contacts must be formed between the GaAs and the wiring metals. Electrical isolation is provided on the sides of the transmission line by mesa etching and between RTDs by proton bombardment. Fabrication of this and similar circuits has begun on 3-in. GaAs substrates.

C. L. Dennis
E. R. Brown
S. Prasad*

*Author not at Lincoln Laboratory.

REFERENCES

1. D. G. Jeng, H. S. Tuan, R. F. Salat, and G. J. Fricano, *Appl. Phys. Lett.* **20**, 1868 (1990).
2. S. D. Wolter, B. R. Stoner, J. T. Glass, P. J. Ellis, D. S. Buhaenko, C. E. Jenkins, and P. Southworth, *Appl. Phys. Lett.* **62**, 1215 (1993).
3. Y. Sato, I. Yashima, H. Fujita, T. Ando, and M. Kamo, *Proceedings of New Diamond Science and Technology Second International Conference* (Materials Research Society, Pittsburgh, 1991), p. 371.
4. P. C. Yang, W. Zhu, and J. T. Glass, *J. Mater. Res.* **8**, 1773 (1993).
5. W. Zhu, P. C. Yang, and J. T. Glass, *Appl. Phys. Lett.* **63**, 1640 (1993).
6. J. T. Glass, private communication.
7. M. Yoder, private communication.
8. M. W. Geis, *Proceedings of Diamond, SiC, and Related Wide Bandgap Semiconductors*, Vol. 62 (Materials Research Society, Pittsburgh, 1990), p. 15.

5. HIGH SPEED ELECTRONICS

5.1 EFFECTS OF RESIST GEOMETRY ON GaAs/AlGaAs STRUCTURES ETCHED WITH ANGLED Cl_2-IBAE

Etch-specific resist geometries have been developed for chlorine ion-beam-assisted etching (Cl_2-IBAE). Our goals were to optimize sidewall smoothness at a variety of sidewall angles and to demonstrate a new process that allows the width of the etched opening to be significantly smaller than that of the resist opening. In the work reported here, we have produced etched slots 80 nm wide with electron-beam resist openings of 200 nm.

The basic Cl_2-IBAE process, described by Geis et al. [1], has been used to micromachine a variety of profiles in GaAs/AlGaAs [2]–[5]. Chlorine from two jets and an Ar^+ ion beam from a separately controlled Kaufman source impinge simultaneously upon a sample. Since neither GaAs nor AlGaAs is appreciably affected by chlorine at room temperature, the slope angle of the etched sidewalls is determined essentially by the incident angle of the Ar^+ beam. Almost any concave shape can be generated using the computer-controlled sample stage, which precisely varies the tilt angle between the sample and the Ar^+ beam during the etch process [6].

The height of the resist, geometry of the resist sidewall, smoothness of the resist edge, and width of the opening in the resist are all interdependent and are interrelated with the etching angle desired and the Cl_2-IBAE process. Figure 5-1 shows the resist properties that must be controlled in order to etch smooth vertical sidewalls. As shown in Figure 5-1(a), edge ripple, sidewall slope, and the resist foot require specific attention. The ripple arises when irregularities in the edges of the photolithographic mask are transferred into the resist pattern. The extraneous foot is created by errors in either exposure or development. The sidewall slope is a function of the resist chemistry, the bake conditions, and the exposure procedure and time. The scanning electron micrograph (SEM) in Figure 5-1(b) shows a resist with all of the features in Figure 5-1(a), except the extraneous foot. A sketch and an SEM of the resulting etched structure are shown in Figures 5-1(c) and 5-1(d), respectively. The mask edge ripple is copied into the sidewall of the etched trench, and after a period of time the hard skin of the resist begins to etch, causing the resist to recede. This recession produces the edge erosion.

We have found that, with careful layout and processing, 4× chrome optical masks can be made with extremely smooth, straight edges. By using these masks in a 4:1 projection printer along with AZ5214E photoresist, we are able to consistently produce the resist structure shown in Figure 5-2(a). Notice that a large portion of the resist sidewall is vertical, that the edge is smooth, and that there is no foot. Figure 5-2(b) shows the extremely smooth vertical sidewall of a structure etched with this type of mask.

To produce smooth angle-etched patterns in GaAs/AlGaAs structures, the resist sidewall must be parallel or nearly parallel to the direction of the ion beam. Fortunately, the closer the resist edge comes to being parallel to the beam the longer it takes to break through the hard resist skin. Good results can usually be obtained within a reasonable range of etch times and sidewall-to-beam angles. In angled etching we use resists with either positively or negatively sloping sidewalls, depending on which is needed.

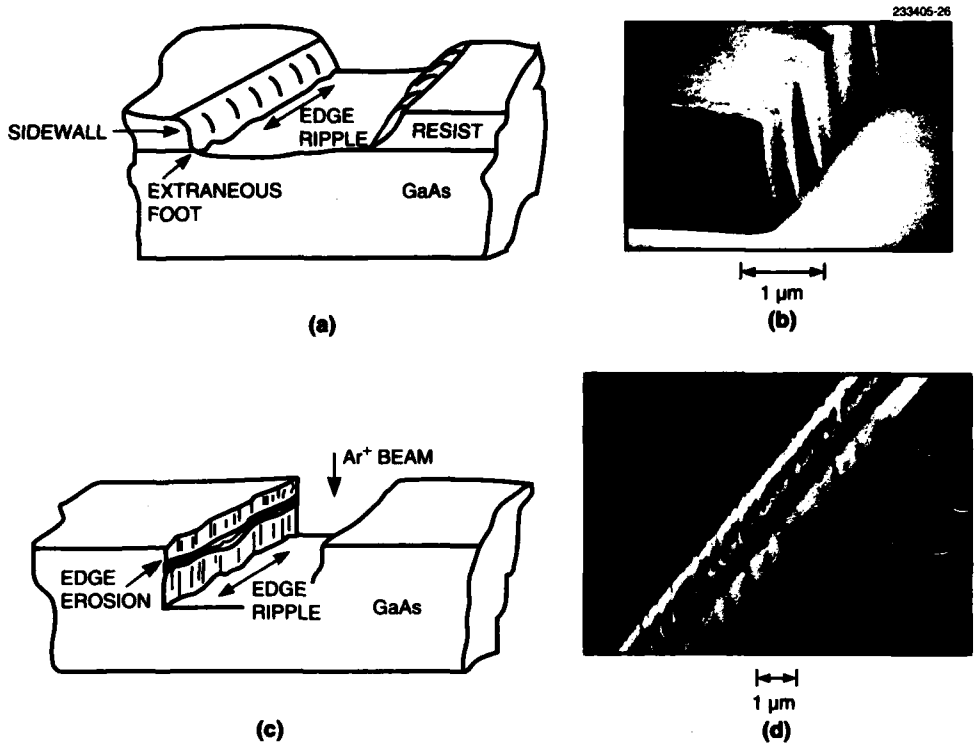

Figure 5-1. Sketches and scanning electron micrographs (SEMs) showing important resist parameters and their effect on the etching process. (a) Diagram and (b) SEM showing resist edge ripple and sloped sidewalls; also seen in (a) is an extraneous foot. (c) Diagram and (d) SEM showing edge erosion and edge ripple produced in the GaAs after etching the structure in (a).

Figure 5-3 sketches two important cases of angle etching through a small resist opening. In the first example, shown in Figure 5-3(a), the resist is rounded and the opening is larger than the height of the resist. As seen, the sidewalls in the GaAs/AlGaAs structure etch parallel to each other. In this case, care must be taken to minimize etch time (depth), so as to minimize erosion of the thin resist edge on the left. A cross section of a structure etched under these conditions is shown in Figure 5-4(a).

In the second example, shown in Figure 5-3(b), openings can be etched that are smaller than the resist opening, because the resist shadows some of the open area with respect to the Ar^+ ion beam. Note that the etched opening in the sample is determined by the area directly bombarded by Ar^+ ions and that the retrograde profile on the shadowed side is caused by the oxide on the GaAs in the shadowed area masking Ar^+ ions that reflect off the resist wall. The key to this process is that the Ar^+ ions reflected off the resist wall do not have sufficient energy to remove the native oxide in the resist opening. The profile

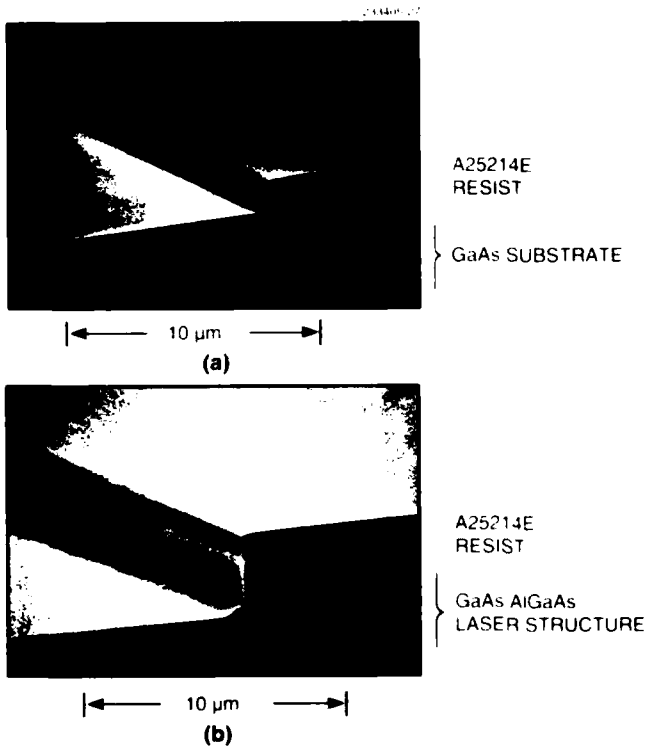

Figure 5-2. SEMs of (a) AZ5214E resist printed using chlorine ion-beam-assisted etching (Cl_2-IBAE) techniques and (b) sidewall of structure etched using the resist as a mask.

of a structure etched using the technique in Figure 5-3(b) is shown in Figure 5-4(b). This profile is ideally suited for knife-edge cathode structures. Either side of the structure can be used as the cathode, and the distance between the cathode and gate can be as small as 40 nm for resist openings as wide as 200 nm. For the structure shown in Figure 5-4(b), we used an 800-nm-thick electron-beam resist, an 8° (from normal) ion-beam angle, and a 200-nm opening to produce an 80-nm cathode-to-gate spacing. The shadowing effect disappears at normal incidence, as demonstrated by Figure 5-4(c), which shows a structure etched using typical conditions at normal incidence and a resist that was much thicker than the openings in the resist.

W. D. Goodhue
R. J. Bailey
J. P. Donnelly
G. D. Johnson
G. A. Lincoln

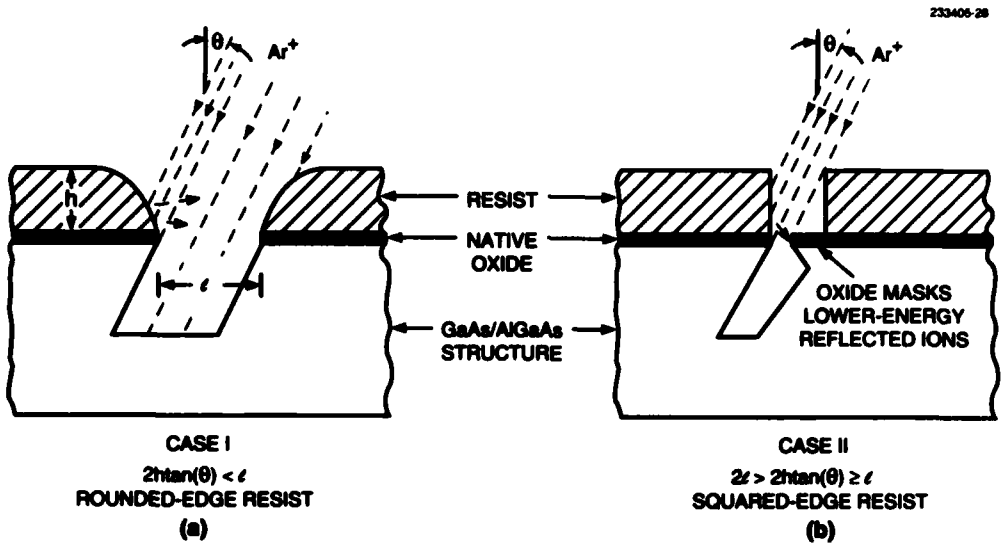

Figure 5-3. Schematic diagrams showing effect of resist geometry on Cl_2-IBAE etching of small structures. In (a) reflected ions do not significantly contribute to the sidewall slope, as compared to (b) where they aid in forming a structure useful in vacuum-microelectronics applications.

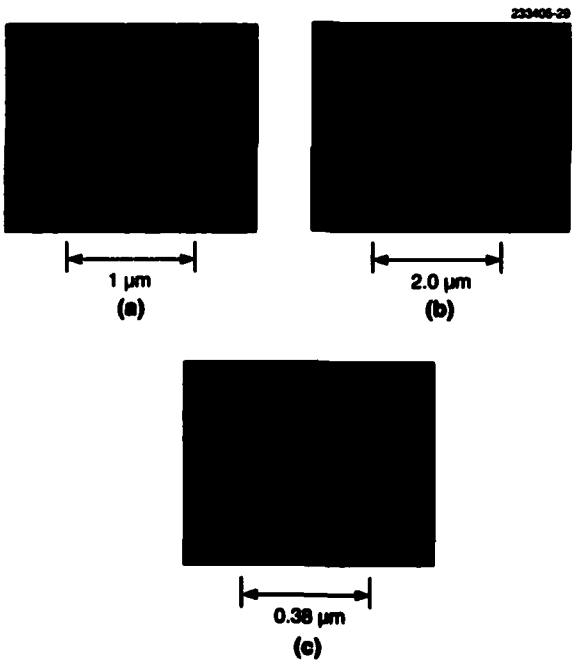

Figure 5-4. SEMs demonstrating ability of Cl_2-IBAE system to etch the structures illustrated in Figure 5-4. Shown are structures obtained using (a) angled etching with a rounded-edge resist, (b) angled etching with a vertical-edge resist whose thickness was greater than the resist opening, and (c) normal-incidence etching with a resist whose thickness was greater than the resist openings. In (b) a 200-nm-wide resist opening was used to produce the 80-nm-wide etched opening.

REFERENCES

1. M. W. Geis, G. A. Lincoln, N. Efremow, and W. J. Piancentini, *J. Vac. Sci. Technol.* **19**, 1390 (1981).
2. J. P. Donnelly, W. D. Goodhue, C. A. Wang, R. J. Bailey, G. A. Lincoln, G. D. Johnson, L. J. Missaggia, and J. N. Walpole, *IEEE Photon. Technol. Lett.* **5**, 1146 (1993).
3. J. P. Donnelly, W. D. Goodhue, C. A. Wang, R. J. Bailey, G. A. Lincoln, G. D. Johnson, L. J. Missaggia, and J. N. Walpole, *IEEE Photon. Technol. Lett.* **5**, 747 (1993).
4. D. E. Bossi, R. W. Ade, R. P. Basilica, and J. M. Berak, *IEEE Photon. Technol. Lett.* **5**, 166 (1993).
5. S. G. Bandy, C. K. Nishimoto, C. Webb, G. Virshup, M. Riaziat, L. Partain, C. Yuen, and C. Shih, *Proceedings of Vacuum Electronics Annual Review* (Naval Research Laboratory, Washington, D.C., 1993), p. VI-37.
6. W. D. Goodhue, G. D. Johnson, and T. W. Windhorn, *Gallium Arsenide and Related Compounds 1986, Inst. Phys. Conf. Ser.* **83**, 349 (1987).

6. MICROELECTRONICS

6.1 WAFER-SCALE 1960 × 2560 FRAME-TRANSFER CCD IMAGER

Applications using broad-area electronic imaging, such as space surveillance and astronomy, have requirements for very large charge-coupled device (CCD) arrays. In the past the desired pixel counts and die area for these arrays severely stressed the fabrication technology, and this in turn forced development of arrays of carefully aligned and closely spaced imager chips. However, the packaging technology for such arrays can be difficult, particularly for space surveillance where the gaps between chips must amount to no more than 3–4 pixels. Silicon IC fabrication technology, on the other hand, continues to demonstrate progressively lower defect counts, and thus the practical die sizes for CCDs have grown rapidly in recent years. We describe here a 5-Mpixel CCD imager, developed for visible-band space surveillance for the GEODSS Upgrade Prototype System (GUPS) and the GEODSS Modification Program (GMP). This device, which occupies an entire 100-mm-diam wafer, is intended to replace the ebsicon tubes currently used in the operational GEODSS sites.

The imager is depicted schematically in Figure 6-1, and a photograph of a completed device is shown in Figure 6-2. The device is designed with a frame-transfer format, with the two upper quadrants of the imaging area clocked upward and the two lower quadrants downward to frame-store buffers. The imaging area comprises 1960 × 2560 pixels with pixel dimensions of 24 × 24 μm. In the GEODSS system, however, the device will primarily be operated with 2 × 2-pixel binning for an effective resolution of 980 × 1280 pixels. The 47 × 61-mm imaging area has a diagonal length of 77.4 mm, which matches well with the 80-mm circular focal-plane diameter of the GEODSS telescopes. The four frame-store buffers, each having 980 × 1280 pixels, are tapered to maintain a prescribed distance between the active portion of the CCD and the wafer edge. Each frame store delivers charge to a serial register which has output circuits on both ends. These registers can be clocked to deliver all the charge to either output, or half the charge can be clocked to the left and half to the right output port. The device can therefore be operated in either an eight- or four-port mode. Although the standard GEODSS frame period is 0.6 s, the device was designed for frame rates up to 10 Hz, and this in turn meant that the output circuit design be capable of sensing charge at a 2-MHz rate in the eight-port mode.

Another feature of this device is two small 32 × 32 frame-transfér imagers located on either side of the imaging area. These small imagers are to be used as high-frame-rate (1000 Hz) photometers to study rotating or tumbling space objects. In this application the telescope boresight is shifted to bring the object of interest into the field of view of either photometer, and the temporal variation in optical signal is recorded. These small imagers will replace a complicated mechanical assembly in the current system, in which an arm moves a beam splitter into the optical path in front of the ebsicon and reflects a portion of the light to a GaAs photomultiplier tube.

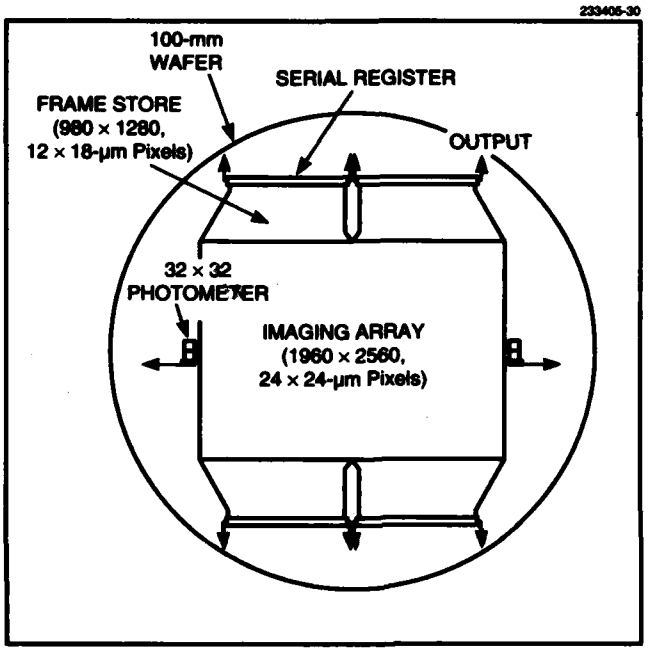

Figure 6-1. Schematic of 1960 × 2560-pixel frame-transfer charge-coupled device imager. This device fills almost all the usable area of a 100-mm-diam silicon wafer.

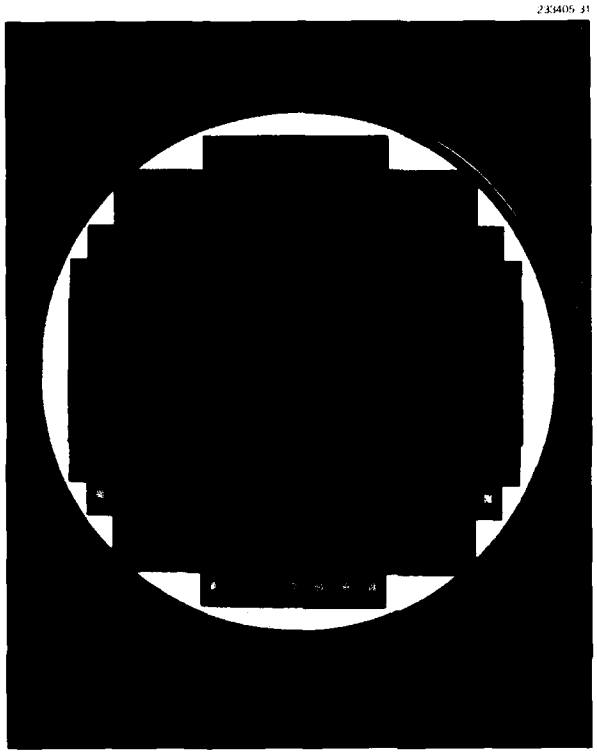

Figure 6-2. Photograph of completed device wafer. Small test structures are located around the periphery of the imager.

This CCD imager has been fabricated using our standard triple-polysilicon, single-level metal, *n*-buried-channel process on 100-mm wafers. The first lot of 22 wafers has been completed and is currently being tested for gate-gate and gate-substrate shorts. Five of the first 11 wafers are free of these defects, which is a higher yield than we anticipated from projections based on smaller chips.

B. E. Burke
R. W. Mountain
D. J. Young

7. ANALOG DEVICE TECHNOLOGY

7.1 MICROWAVE POWER-HANDLING CAPABILITY OF SUPERCONDUCTING PLANAR TRANSMISSION LINES AND RESONATORS

Successful demonstrations of high-performance superconducting devices in high-power applications such as output-filter and antenna-feeding networks will greatly enhance the possibility of commercialization of superconducting devices. The maximum power-handling capability of a passive microwave superconducting device is limited by the maximum magnetic field that can be tolerated at the surface of the superconductor. When the peak magnetic field is greater than the critical field, flux penetrates the superconductor causing a dramatic increase in loss. Here, we summarize calculations and comparisons of the power-handling capability of transmission-line structures such as microstrip lines, striplines, and coplanar waveguides as well as resonating structures based upon these transmission lines, and microstrip disk resonators.

The geometries considered in this work are shown in Figure 7-1. The analysis was performed for transmission lines and resonators of 0.4-μm-thick Nb on 508-μm-thick $LaAlO_3$ substrate with $\varepsilon_r = 23.5$ and $\tan \delta = 2 \times 10^{-6}$ at 4.2 K. For striplines the separation of the ground planes is 1016 μm; for coplanar waveguide structures the width of each ground plane is 600 μm. The parameters used for Nb and the dimensions of the structures are summarized in Table 7-1.

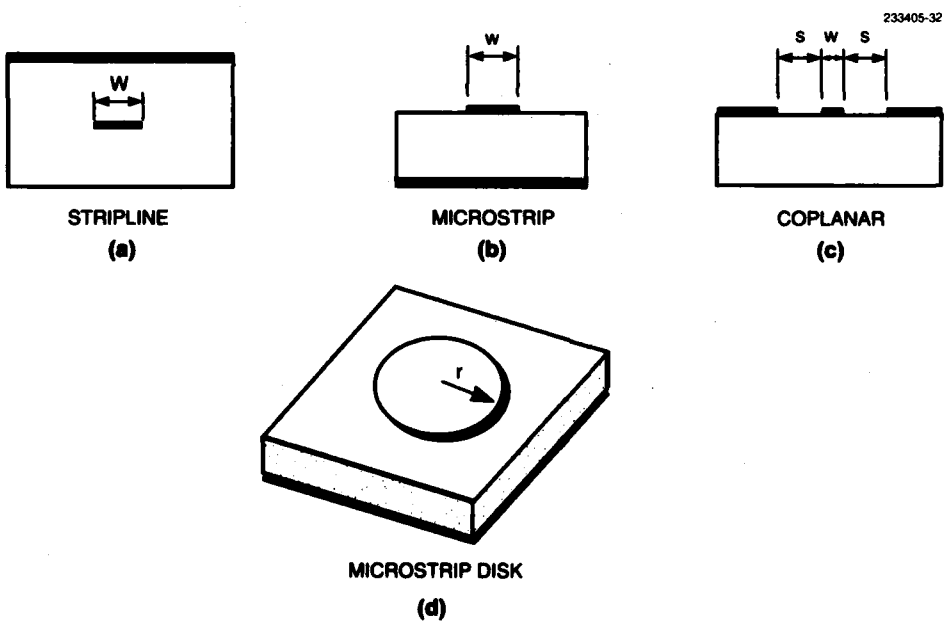

Figure 7-1. Geometries of superconducting resonators: (a)–(c) Cross-sectional views of linear half-wavelength resonators and (d) rotated view of microstrip disk resonator.

TABLE 7-1

Parameters for Transmission Lines and Resonating Structures*

Structure†	w (μm)	s (μm)	Z_0 (Ω)	Mode	r (cm)
MS15	1800	—	~15	—	—
MS50	181	—	~50	—	—
MS86	20	—	~86	—	—
CPW50-50	50	87.5	~50	—	—
CPW86-20	20	355	~86	—	—
CPW50-20	20	35	~50	—	—
SL40	101	—	~40	—	—
SL50	43	—	~50	—	—
DK0	—	—	—	0	1.89
DK1	—	—	—	1	0.91

*For Nb, T_c = 9.25 K, T = 4.2 K, $\lambda(0)$ = 0.07 μm, and $\sigma_1(T_c)$ = 3000 S/μm.

†MS indicates microstrip, CPW coplanar waveguide, SL stripline, and DK microstrip disk.

The spectral-domain volume-integral-equation method [1],[2] is used to calculate the current density distribution for microstrip lines and coplanar waveguides, while the modified Weeks method [3] is employed for stripline structures. From the current density distribution, the peak magnetic field can be calculated. The maximum current and hence the maximum power that can be carried by the transmission line occur when the peak magnetic field at the surface reaches a critical field at which some parameter attains its maximum permissible value. To eliminate the dependence on the value of the critical field the maximum power is normalized with respect to that for structure SL50 (see Table 7-1). A comparison of calculated power-handling capability at 2 GHz for various transmission lines is listed in Table 7-2. For the 50-Ω transmission line a microstrip structure has more than four times the power-handling capability of a stripline structure. Superconducting coplanar waveguide structures can have similar power-handling capability to microstrip structures (MS86 and CPW86-20), but the large spacing from strip to ground plane for such coplanar waveguide structures may make them impractical for certain applications. Thus, microstrip resonators are superior to the other transmission-line resonators considered here.

TABLE 7-2

Relative Power-Handling Capability of Superconducting Transmission Lines

Structure†	Z_0 (Ω)	Normalized Maximum Power
MS15	15	18
MS50	50	4.1
MS86	86	0.81
CPW50-50	50	1.1
CPW86-20	86	0.81
CPW50-20	50	0.46
SL40	40	1.9
SL50	50	1.0

Various resonating structures have been used to construct superconducting microwave filters [4]. A high-Q resonating structure is required to build high-performance narrowband filters. This Q for several commonly used half-wavelength transmission-line resonators and microstrip disk resonators is calculated and shown in Table 7-3. Radiation losses were not included in the calculation of the Q, since these can be prevented by enclosing a resonator inside a box having modes at frequencies different from those of the resonator. Also shown in Table 7-3 is the ratio R_E of total energy stored to peak energy density at the superconductor surface. Since R_E is proportional to the power circulating in the resonator, i.e., I^2, divided by the square of the peak magnetic field at the superconductor surface required to reach the current I, a larger R_E for a structure implies that it can handle higher circulating power for a given critical field. The calculated R_E for the structures is summarized in Table 7-3. The results for the microstrip disk resonators are calculated using the field solutions given in [5]. Because of its physical volume and the absence of current peaks at the edge of the structure, a microstrip disk resonator has a much higher power-handling capability than transmission-line resonating structures.

L. H. Lee*
W. G. Lyons
T. P. Orlando*

*Author not at Lincoln Laboratory.

TABLE 7-3

Quality Factor and Power-Handling Capability of Superconducting Resonating Structures with f_0 = 2 GHz*

Structure	Q_c	$1/(1/Q_c + 1/Q_d)$	R_E (cm^3)
DK0	1.37×10^6	3.67×10^5	0.27
DK1	1.37×10^6	3.67×10^5	0.18
MS15	1.06×10^6	3.40×10^5	1.3×10^{-5}
MS50	2.02×10^5	1.44×10^5	3.3×10^{-6}
MS86	4.80×10^4	4.38×10^4	6.4×10^{-7}
CPW50-50	4.66×10^4	4.26×10^4	8.6×10^{-7}
CPW86-20	4.40×10^4	4.04×10^4	6.3×10^{-7}
CPW50-20	2.06×10^4	1.98×10^4	3.5×10^{-7}
SL40	1.20×10^5	9.68×10^4	1.5×10^{-6}
SL50	7.14×10^4	6.25×10^4	7.9×10^{-7}

*Q_c and Q_d are the conductor and dielectric Q, respectively, and R_E is the ratio of the total stored energy to the peak energy density.

REFERENCES

1. L. H. Lee, S. M. Ali, and W. G. Lyons, *IEEE Trans. Appl. Superconduct.* **2**, 49 (1992).
2. L. H. Lee, S. M. Ali, W. G. Lyons, D. E. Oates, and J. D. Goette, *IEEE Trans. Appl. Superconduct.* **3**, 2782 (1993).
3. D. M. Sheen, S. M. Ali, D. E. Oates, R. S. Withers, and J. A. Kong, *IEEE Trans. Appl. Superconduct.* **1**, 108 (1991).
4. N. Newman and W. G. Lyons, *J. Superconduct.* **6**, 119 (1993).
5. J. Watkins, *Electron. Lett.* **5**, 524 (1969).

REPORT DOCUMENTATION PAGE

Form Approved
OMB No. 0704-0188

Public reporting burden for this collection of information is estimated to average 1 hour per response, including the time for reviewing instructions, searching existing data sources, gathering and maintaining the data needed, and completing and reviewing the collection of information. Send comments regarding this burden estimate or any other aspect of this collection of information, including suggestions for reducing this burden, to Washington Headquarters Services, Directorate for Information Operations and Reports, 1215 Jefferson Davis Highway, Suite 1204, Arlington, VA 22202-4302, and to the Office of Management and Budget, Paperwork Reduction Project (0704-0188), Washington, DC 20503.

1. AGENCY USE ONLY (*Leave blank*)	2. REPORT DATE	3. REPORT TYPE AND DATES COVERED
	15 November 1993	Quarterly Technical Report, 1 August – 31 October 1993

4. TITLE AND SUBTITLE

Solid State Research

5. FUNDING NUMBERS

C — F19628-90-C-0002
PE — 63250F
PR — 221

6. AUTHOR(S)

Alan L. McWhorter

7. PERFORMING ORGANIZATION NAME(S) AND ADDRESS(ES)

Lincoln Laboratory, MIT
P.O. Box 73
Lexington, MA 02173-9108

8. PERFORMING ORGANIZATION REPORT NUMBER

1993:4

9. SPONSORING/MONITORING AGENCY NAME(S) AND ADDRESS(ES)

HQ Air Force Materiel Command
AFMC/STSC
Wright-Patterson AFB, OH 45433-5001

10. SPONSORING/MONITORING AGENCY REPORT NUMBER

ESC-TR-94-084

11. SUPPLEMENTARY NOTES

None

12a. DISTRIBUTION/AVAILABILITY STATEMENT

Approved for public release; distribution is unlimited.

12b. DISTRIBUTION CODE

13. ABSTRACT (*Maximum 200 words*)

This report covers in detail the research work of the Solid State Division at Lincoln Laboratory for the period 1 August through 31 October 1993. The topics covered are Electrooptical Devices, Quantum Electronics, Materials Research, Submicrometer Technology, High Speed Electronics, Microelectronics, and Analog Device Technology. Funding is provided primarily by the Air Force, with additional support provided by the Army, ARPA, Navy, BMDO, and NASA.

14. SUBJECT TERMS

electrooptical devices
quantum electronics
materials research
submicrometer technology
high speed electronics
microelectronics
analog device technology
lasers
epitaxial growth
diamond films
resonant-tunneling transmission lines
charge-coupled imagers
superconductive microwave structures

15. NUMBER OF PAGES
70

16. PRICE CODE

17. SECURITY CLASSIFICATION OF REPORT	18. SECURITY CLASSIFICATION OF THIS PAGE	19. SECURITY CLASSIFICATION OF ABSTRACT	20. LIMITATION OF ABSTRACT
Unclassified	Same as Report	Same as Report	Same as Report

NSN 7540-01-280-5500

Standard Form 298 (Rev. 2-89)
Prescribed by AMSI Std. 239-18
298-102